DEVELOPMENT AND UTILIZATION OF MAGNETICALLY ACTUATED MILLI-SWIMMERS BY STEREOLITHOGRAPHY

Begüm Hira DOMAÇ

FEBRUARY 2022

DEVELOPMENT AND UTILIZATION OF MAGNETICALLY ACTUATED MILLI-SWIMMERS BY STEREOLITHOGRAPHY

A THESIS SUBMITTED TO THE

GRADUATE SCHOOL

OF

BAHÇEŞEHİR UNIVERSITY

BY

BEGÜM HİRA DOMAÇ

IN PARTIAL FULFILLMENT OF THE REQUIREMENTS

FOR

THE DEGREE OF MASTER OF BIOMEDICAL ENGINEER

IN THE DEPARTMENT OF BIOMEDICAL ENGINEERING

FEBRUARY 2022

BAHCESEHIR UNIVERSITY

GRADUATE SCHOOL

28/01/2022

MASTER THESIS APPROVAL FORM

Program Name:	Graduate Program of Biomedical Engineering
Student's Name and Surname:	Begüm Hira Domaç
Name Of The Thesis:	Development and Utilization of Magnetically Actuated Milli-swimmers by Stereolithography
Thesis Defense Date:	28.01.2022

This thesis has been approved by the Graduate School which has fulfilled the necessary conditions as Master thesis.

Prof. Dr. Ahmet ÖNCÜ

Institute Director

This thesis was read by us, quality and content as a Master's thesis has been seen and accepted as sufficient.

	Title/Name	**Signature**
Thesis Advisor	Assoc. Prof. Ozan Akdoğan	
Thesis Co-advisor	Asst. Prof. Ahmet Fatih Tabak	
1st Member	Asst. Prof. Hakan Solmaz	
2nd Member	Asst. Prof. Bora Büyüksaraç	
3rd Member	Asst. Prof. Nilay Gündüz Akdoğan	

I hereby declare that all information in this document has been obtained and presentedin accordance with academic rules and ethical conduct. I also declare that, as requiredby these rules and conduct, I have fully cited and referenced all material and results that are not original to this work.

Name, Surname : Begüm Hira Domaç

Signature :

ABSTRACT

DEVELOPMENT AND UTILIZATION OF MAGNETICALLY ACTUATED MILLI-SWIMMERS BY STEREOLITHOGRAPHY

Domaç, Begüm Hira
Biomedical Engineering Masters Program
Supervisor: Assoc. Prof. Dr. Ozan Akdoğan

February 2022, 46 pages

Magnetic nanoparticles are key components in many fields of science and industry. Especially in cancer diagnosis and therapy, they are involved in targeted drug delivery and hyperthermia applications due to their ability to be controlled remotely. The hyperthermia method ensures that the cancer cells in the targeted area are inactive.

Within the scope of the project, the Stereolithography (SLA) 3D printing technique is used in which magneto-sensitive swimmers loaded with a variety of magnetic particles are obtained. Magneto-sensitive milli and sub-milli-swimmers exhibited various movements and trajectories in the liquid medium under the magnetic field gradient. An object detection algorithm was merged with the electromagnetic coil mechanism for the position information of the swimmers. In addition, the MATLAB environment was developed to simulate the movements of swimmers under a magnetic field gradient. The magnetic particles' localized heat effect (hyperthermia) was tested using an induction heater. The prototype system has been developed and presented for connecting small-scale swimmers with minimally invasive biomedical applications.

Keywords: Nanoparticles, Magneto-responsive Swimmers, 3D printing, Real-Time Swimmer Detection, Hyperthermia.

ÖZ

MANTETİK AKTİVASYONLU MİLİMETRİK YÜZÜCÜLERİN STEREOLİTOGRAFİ İLE GELİŞTİRİLMESİ VE KULLANILMASI

Domaç, Begüm Hira
Biyomedikal Mühendisliği Lisansüstü Programı
Supervisor: Doç.Dr. Ozan Akdoğan

Şubat 2022, 46 sayfa

Manyetik nanoparçacıklar, bilim ve endüstrinin birçok alanında anahtar bileşenlerdir. Özellikle kanser tanı ve tedavisinde, uzaktan kontrol edilebilmeleri nedeniyle hedefe yönelik ilaç verme ve hipertermi uygulamalarında yer almaktadırlar. Hipertermi yöntemi, hedeflenen bölgedeki kanser hücrelerinin inaktif olmasını sağlar.

Proje kapsamında, çeşitli manyetik parçacıklar yüklü manyeto-duyarlı yüzücülerin elde edildiği Stereolitografi (SLA) 3D baskı tekniği kullanılmıştır. Manyetik olarak duyarlı milimetrik yüzücüler, sıvı ortamda manyetik alan gradyanı altında çeşitli hareketler ve yörüngeler sergilediler. Yüzücülerin konum bilgileri için bir nesne algılama algoritması elektromanyetik bobin mekanizması ile birleştirildi. Ayrıca MATLAB ortamı, yüzücülerin hareketlerini bir manyetik alan gradyanı altında simüle etmek için geliştirilmiştir. Manyetik parçacıkların lokalize ısı etkisi (hipertermi), bir endüksiyon ısıtıcı kullanılarak test edildi. Küçük ölçekli yüzücüleri minimal invaziv biyomedikal uygulamalarla birleştirmek için prototip sistem geliştirilmiş ve sunulmuştur.

Anahtar Kelimeler: Nanoparçacıklar, Manyetik-duyarlı yüzücüler, 3D baskı, Gerçek Zamanlı Yüzücü Takibi, Hipertermi.

To my champion father
and my beloved mother,
Yıldıray and Aysun
Domaç

ACKNOWLEDGMENTS

First and foremost, I would like to express my sincere gratitude to my dear supervisor Assoc. Prof. Dr. Ozan Akdoğan for his guidance, support, and appreciation at every stage of this thesis. The thesis was accomplished with his help. I am deeply grateful to Dr. Ahmet Fatih Tabak and Dr. Bora Büyüksaraç for their guidance, insightful comments, and suggestions. I would like to thank Dokuz Eylül University Center for Fabrication of Electronic Materials, Sabancı University Center of Excellence for Functional Surfaces and Interfaces, and MSG Electric.

I would also like to offer my special thanks to my lab colleagues; Sedef Özünlü, Lorin Doğantürk, and Hayder Al-Shammari, for their contribution and responding to my questions tirelessly. I would like to extend my sincere thanks to Mustafa Can Kurt for perfecting the live detection system.

Lastly, I owe a lot of thanks to my unique friends for their encouragement throughout the process but most importantly, none of this could have happened without my family.

This work was supported by BAP.2021.01.17 (Bahcesehir University).

Istanbul, 2022 Begüm Hira DOMAÇ

TABLE OF CONTENTS

LIST OF FORMULAS

FORMULAS

LIST OF TABLES

TABLES

LIST OF FIGURES

FIGURES

LIST OF ABBREVIATIONS

3D	Three dimensional
AC	Alternating Current
BCC	Body-centered Cubic
FCC	Face-centered Cubic
HCP	Hexagonal Close Packed
FDA	Food and Drug Administration
FCT	Face-centered Tetragonal
EMF	Electromotive Force
SLA	Stereolithography
DLP	Digital Light Processing
UV	Ultraviole.
PDMS	Polydimethylsiloxane
LOC	Lab-on-a-chip
SAR	Specific Absorption Rate
OA	Oleic Acid
PEG	Polyethylene Glycol
OAm	Oleylamine
SEM	Scanning Electron Microscope
CAD	Computer Aided Design
STL	Standard Triangle Language
OpenCV	Open-Source Computer Vision Library
GPU	Graphics Processing Unit
VSM	Vibrating Sample Magnetometer
XRD	X-Ray Diffraction
IR	Infrared
TEM	Transmission Electron Microscope
DI	Distilled

CHAPTER 1

INTRODUCTION

With the development of three-dimensional (3D) printing, robust and promising structures are obtained by utilizing extrusion-based and light-assisted methods. (Tetsuka & Shin, 2020) Among the latest developments, the rapid prototyping method, advantageous in time efficiency, provides a functional area of use by obtaining models with novel 3D geometric shapes. (Melchels et al., 2010) To increase the capabilities of the small-scale devices obtained with this production method, they require collaboration in an integrated manner with functional nano/micro materials depending on the industry. (S. Kim et al., 2020) The nanoparticle embedded resin matrix could be used to 3D print robot/swimmers by additive manufacturing technique. (Weng et al., 2016)

The recent developments in material science and nanotechnology triggered nanoparticle-based treatment methods in medicine. (Jun et al., 2008; Niemirowicz et al., 2012) In particular, magnetic nanoparticles with their low toxicity, biocompatibility, biodegradability, and magnetic properties are actively used to diagnose and treat cancer; MRI-magnetic imaging, hyperthermia, and controlled drug delivery. (Belyanina et al., 2017; Hossen et al., 2019; Taukulis et al., 2015; Vallabani & Singh, 2018) Since the tracking and control mechanisms of the particles on the nanoscale are limited, multi-functional swimmers have been developed on milli/microscales. (Gallego-Urrea et al., 2011; Hu et al., 2018; Sitti et al., 2015) The integration of micro and nanoparticles into functional systems such as small-scale robots/swimmers in terms of drug and treatment strategies has shown excellent potential. (Koleoso et al., 2020; Llacer-Wintle et al., 2021; Peer et al., 2007; Sanchez et al., 2011a) The small-scale robots and swimmers can perform complex maneuvers in harsh environments, lab-on-a-chip applications, and perform several locomotion tasks. Several types of actuation methods could be used to trigger the movement of these swimmers: chemical propulsion, swimming, magnetic gradient pulling, and biological cell propulsion. (Sitti et al., 2015) Magnetic swimmers can interact harmoniously with the human body and release drugs to the targeted area through magnetic torque control, utilizing the magnetic actuation principle. (S. H. Kim & Ishiyama, 2014) Furthermore, under the effect of

these magnetic forces, swimmers could create an apoptosis mechanism by directly providing heat to tumor tissues by using an alternating magnetic field. (Ramos-Docampo et al., 2019) Several methods are available for controlled heat therapy: optical heating and ultrasound heating, and heating of magnetic particles under an alternating (AC) magnetic field. (Abenojar et al., 2016; Beik et al., 2016)

In this research, 3D printed milli-swimmers have been synthesized by the stereolithography method. Three different magnetic particles were embedded in the resin matrix. A real-time control system has been developed which monitors the drift/movement of swimmers in the liquid medium under an externally applied magnetic field gradient. To optimize the magnetic and hydrodynamic properties of the synthesized swimmers, their trajectories were simulated using MATLAB. The heat emitted by particles exposed to an alternating magnetic field with an induction coil is measured with a calorimeter. The research on these unique trajectories, speeds of the multifunctional swimmers, and the designed control system have the potential to benefit many challenges in the biomedical industry, especially magnetic hyperthermia-based treatment methods.

CHAPTER 2

LITERATURE REVIEW

Recently, magnetic particle-integrated swimmers have gathered great attention, which could manipulate hard-to-reach areas with an externally applied control mechanism. (Ceylan et al., 2017) Among the robots/swimmers, magnetically configured ones are pretty advantageous due to their flexible maneuver skills. (Abbott et al., 2009) Untethered magnetic small-scale swimmers have been used in treatment and diagnosis in the biomedical field; they can exhibit complex movement mechanisms. (Ceylan et al., 2019; S. H. Kim & Ishiyama, 2014) Several types of particles with different magnetic properties have been used to synthesize magnetically actuated swimmers: ferromagnetic (Darmawan et al., 2019) and superparamagnetic materials. (Goudu et al., 2020) The 3D printing approach has been applied to synthesize small-scale structures time efficiently and economically. (Kitson et al., 2012; Liu & Mo, 2010) Recently developed 3D-printed swimmers have various movements and motion trajectories, such as rolling and rotation due to their customized structures; helical, (Ceylan et al., 2019) sperm, (Stanton et al., 2015) and spherical shape. (Lee et al., 2020) The complex motion performances of swimmers and their interaction with environmental conditions can be simulated by determining the motion and fluid dynamics equations. (Yasa et al., 2020) Thus, advanced systems can be achieved by computational optimizations.

2.1 MICRO AND NANOPARTICLES

Micro and nanotechnology refer to a group of techniques for fabricating and studying advanced systems with dimensions ranging from nanometers (one nanometer is 10^{-9} meters) to several micrometers (one micrometer is 10^{-6} meters). The bottom-up and top-down approaches are used to synthesize micro and nanoparticles of functionality, morphology, and size. (Hamley, 2003) The particles' magnetic, optical, electrical, and chemical properties could be improved by a decrease in sizes into micro and nano dimensions. (Khan et al., 2011; P. et al., 2016) Nanoparticles have been utilized and developed in various sectors (e.g., engineering, medicine, food, and defense industry).

2.1.1 Iron and Iron Oxide (Fe-O) Nanoparticles. The iron element is a soft ferromagnetic material. It has a high curie temperature of 770 ℃ and a body-centered cubic (BCC) crystal structure. (Dworzanski & Meuzelaar, 2016; Pepperhoff & Acet, 2001) Chemical compounds formed by oxygen and iron exist in various forms such as iron (II) oxide/wüstite (FeO), iron (II, III) oxide/magnetite (Fe_3O_4), and iron (III) oxide/hematite (α-Fe_2O_3). (M. et al., 2011) FeO and Fe_3O_4 have a face-centered cubic (FCC) crystal structure, and α-Fe_2O_3 has hexagonal close-packed (HCP) crystal structures as shown in figure 1. (Parkinson, 2016) Fe_3O_4 (Magnetite) has a curie temperature of ~585 ℃. (Ningthoujam et al., 2012) Various electronic and optical properties can be obtained by changing the size, crystallinity, and morphology of these particles. (Khurshid et al., 2013)

The iron oxide nanoparticles have been used both in diagnostics and therapeutics as a material approved by the US Food and Drug Administration (FDA). (El-Boubbou, 2018; Popescu et al., 2019) Fe/Fe_3O_4 core/shell nanoparticles with 20 nm size are toxic to cancerous cells in vitro. (Domac et al., 2020) These nanoparticles are considered a suitable choice to prevent embolization in medical applications. (Arruebo et al., 2011)

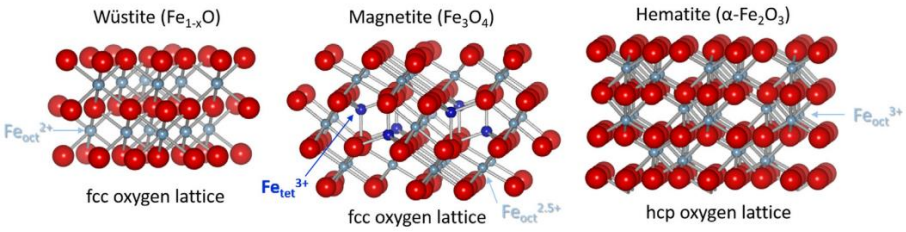

Figure 1 Crystal Structures of Iron Oxide Compounds

(Parkinson, 2016)

2.1.2 Neodymium Iron Boron (NdFeB). Neodymium is a rare earth element in the lanthanide series and has a paramagnetic ordering at room temperature. (Rao et al., 2018) An alloy of Nd, Fe, and B elements is frequently used in manufacturing magnets; it is known that the Neodymium-Iron-Boron permanent magnets (Nd-Fe-B) exhibit excellent magnetic properties shown in the table. (Table 1) (Gutfleisch et al., 2011; Hussain et al., 2016) NdFeB has the curie temperature of 309.85 ℃ and a face-centered tetragonal (FCT)

crystallographic structure shown in figure 2. (Skomski & Sellmyer, 2009; Yang et al., 2018; Yi et al., 2002) On the other hand, Nd-Fe-B particles have been proposed to be integrated into small-size robots due to their hard magnetic properties and effective actuation potentials under the electromagnetic control systems. (Pawashe et al., 2009)

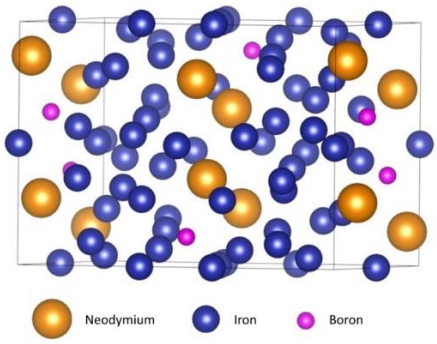

Figure 2 Nd-Fe-B Crystallographic Structure

2.1.3 Fe Flake. The Fe flake is a high-performance magnetic material due to its wide saturation magnetization and anisotropic property. (Table 1) (Zirhli et al., 2020) Flake-shaped particles can increase chemical reactivity due to their high aspect ratio and surface area morphologies. (Theodore, Jeon, and Wu, 2006) The morphologic and magnetic structures of these particles synthesized by the ball milling method can be modified using different surfactants, grinding times, and ball numbers/ratios. (Akdogan, Hadjipanayis, and Sellmyer, 2009) The comparison between the magnetic properties of Nd-Fe-B, Fe, and Fe_3O_4 is presented in Table 1.

Table 1

Magnetic Property Comparison of Materials

Magnetic materials	Curie Point (℃)	Anisotropy	Saturation Magnetization	Crystal Structure
Fe_3O_4	~585 ℃	1.1–1.3 × 10^4 J/m^3	59.1 emu/g	Face-centered cubic (FCC)
Nd-Fe-B	309.85 ℃	5 x 10^3 J/m^3	114 emu/g	Face-centered tetragonal (FCT)
Fe	770 ℃	4.8 × 10^4 J/m^3	212 emu/g	Body-centered cubic (BCC)

2.2 MAGNETISM AND MAGNETIC PROPERTIES

Magnetism has allured the attention of various civilizations from BC to the present. The naturally magnetized mineral, called lodestone, has pioneered the modern explanation of magnetic phenomena. Magnetization occurs through which the orientation of dipole moments aligns in the direction of the magnetic field. The current due to moving electric charges is the origin of the magnetism phenomena. (Griffiths, David J; College, 1999) Specifically, the spinning motion of electrons induces a magnetic field, resulting in a magnetic moment. Therefore, due to the magnetic moment formed in the atomic scale, a magnetic moment also occurs in the magnetic materials. The magnetic properties of the material have been classified according to their reaction to the magnetic field. This property is determined by the ratio of induced magnetization to the applied magnetic field. (C. Sun et al., 2008)

2.2.1 Ferromagnetism. Ferromagnetic materials consist of tiny, magnetized regions: magnetic moment vectors create a magnetic moment in the domains of the substance. (Spain & Venkatanarayanan, 2014) In ferromagnetic materials, vectors are aligned in the same direction with the magnetic field lines of the magnet while exposure of an external magnetic field is illustrated in figure 3. (Goldman, 1999) These materials cause a large net magnetization even without a magnetic field. (Sung & Rudowicz, 2003)

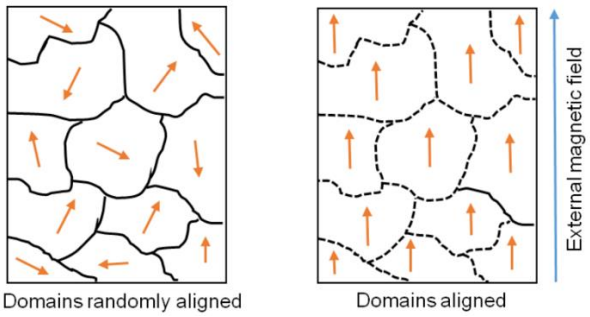

Figure 3 Ferromagnetic Domains in an External Magnetic Field's Absence (left) and Presence (right)
(Nisticò, Cesano and Garello, 2020)

2.2.1.1 Hysteresis Curve

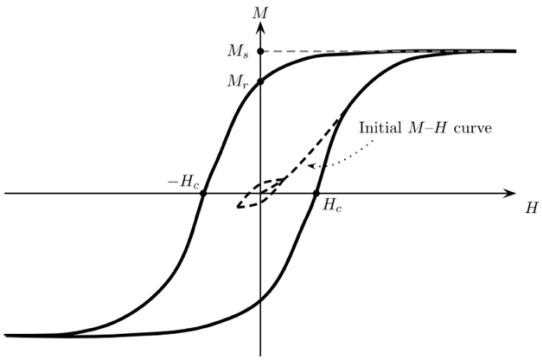

Figure 4 Hysteresis (M-H) Curve

(Aharoni, 2000)

Magnetic hysteresis can be represented as the relationship between a magnetic field (H) and magnetization (M). (figure 4) This curve interprets how a magnetic material interacts with an external magnetic field. The increase in the magnetic field (H) and magnetization (M) would increase until the material reaches the point of saturation magnetism (M_s). When the magnetic field reaches zero, the value of magnetism on the curve shows a residual magnetization. This value is called remanent magnetization (M_r). The magnetization continues to decrease, and at a certain negative applied field where magnetization becomes zero is called the coercivity, H_c. The magnetic field increasing in the opposite direction causes the material to reach magnetic saturation in the negative direction. The curve would be completed when the same values are applied in the opposite direction.

2.2.2 Electromagnetic Induction. The relationship between electric currents and magnetism was first understood by Hans Christian Oersted. Over time, because of the development of this relationship known as electromagnetism, with the discovery of electromagnetic induction by Michael Faraday in 1831, the working principle of the induction coil appeared. Current flowing through a coil creates a magnetic field in and outside of it. The direction of current flow determines the direction of this magnetic field. The alternating current (AC) flowing through the coil causes the magnetic field direction to change at the same rate as the current frequency, thus an AC field is obtained. (Figure 5) An electrically conductive object placed inside the coil causes induced voltage,

and the resistance to the flow of electrons is released as heat. (Pollefliet, 2018) More generally the source of heat generation is caused by eddy current, Brownian and Neel motions, and magnetic hysteresis loss of the workpiece/particles inside the coil. (Deatsch & Evans, 2014; Wu et al., 2020) Further information on the magnetic particle-induced hyperthermia effect is explained in section **2.6**. When the conductive material is exposed to high frequency alternating current manipulation, the electromotive force (EMF) is generated in the induction coil shown in the formula 1. (Vishnuram et al., 2020) This electromotive force depends on the number of turns of a solenoid, N, and magnetic flux, $\boldsymbol{\Phi_B}$.

$$\mathcal{E} = -N\frac{d\,\Phi_B}{dt}$$

Formula 1. The Electromagnetic Induction (Faraday's Law)

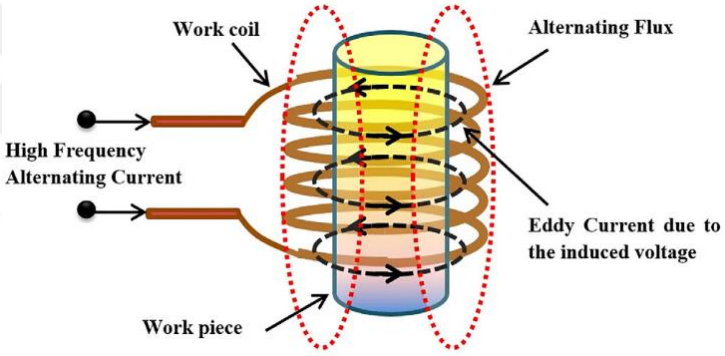

Figure 5 Schematic of Induction Heating

(Vishnuram et al., 2020)

2.2.3 Solenoid. Solenoids consist of wires wrapped helically on a cylinder to create a magnetic field. The electric current passing through a solenoid generates a uniform magnetic field. In formula 2, the magnetic field B is proportional to the electric current l through the solenoid, n illustrates the number of turns of the wire and **μ** is magnetic permeability.

$$\boldsymbol{B = \mu n l}$$

Formula 2. Solenoids' Magnetic Field.

Modified solenoids, which supply efficient alternative magnetic field generation, are frequently used. (Bordelon et al., 2012; Stauffer et al., 1994) Especially considering the heating behavior of the coils, the capacities of the helical solenoids were superior. (Vishnuram et al., 2020)

2.2.3.1 Magnetic Field Gradient Theory. The magnetic field gradient is the magnetic field variation dependence with respect to a position. The magnetic force could be exerted using a magnetic field gradient to move an object through a liquid environment. (Yesin et al., 2006) Objects under the magnetic field are attracted and travel along the field gradient direction when the magnetic moment lines up in the magnetic field direction. (Peyer et al., 2013)

$$\mathbf{F_m} = \nabla(\mathbf{m} \cdot \mathbf{B})$$

Formula 3. Magnetic Force.

In the equation, the magnetic force F_m is the applied force on the objects with magnetic moment m, due to an applied magnetic field B and the gradient ∇ is the variation of the components m and B per unit distance. (formula 3) Especially in magnetic microrobot designs, magnetic actuation could be accomplished using the field gradient. (Abbott et al., 2009)

2.2.3.2 *Drag Force.* The hydrodynamic drag force acts on the objects that maneuver in a liquid medium. In the formula below, η, R and $\boldsymbol{v}$ represent the fluid's viscosity, the hydrodynamic radius of the particle, and the particles' velocity, respectively.

$$\boldsymbol{F_d = 6\pi\eta R v}$$

Formula 4. Drag Force (Stokes' Law).

In addition, drag force can be calculated for the movements of swimmers and robots in the liquid by using the drag coefficient. The coefficient C_d represents the dependence of drag on the objects' surface and geometry. (Aarønæs & Nilsson, 2014) (figure 6) The equation can be expressed as where ρ is the density of the liquid, A is the area of the

robot/swimmer, v is the velocity of the robot/ swimmer, and C_d is the drag coefficient describing the effect of the object's structure on the drag force.

$$F_d = \frac{1}{2}\rho v^2 C_d A$$

Formula 5. Drag Equation.

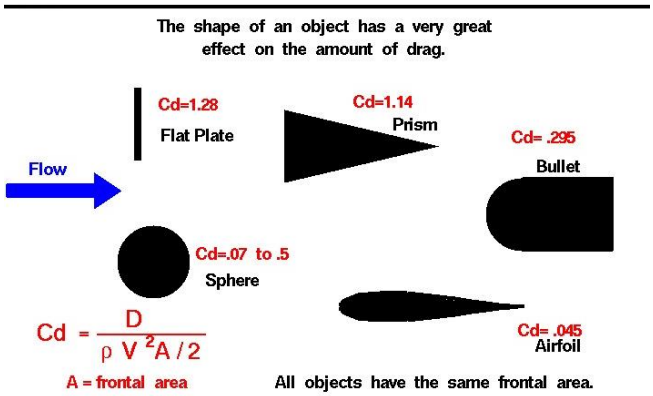

Figure 6 Drag Coefficient for Different Object Shapes (Glenn Research R Center)

2.3 3D PRINTING

In the 1980s, the Stereolithography (SLA) technique was introduced to the literature by Charles W. Hull to develop 3D prototypes. (Hull, 1984) Among the 3D printing methods, stereolithography and digital light processing (DLP) techniques, using ultraviolet (UV) sensitive resin, shorten the photocuring time and allow a resin to be layered to produce functional 3D objects. (Fantino et al., 2016) The top-down light-assisted stereolithography techniques' working process is illustrated in figure 7. The polymerization of the photosensitive resin takes place by bottom irradiation, and structures are formed on the building platform by a top-down approach. Thus, each newly produced layer is placed on top of the previous layer. (Billiet et al., 2012) This technique has been an outstanding predecessor since different prototypes on a small scale have been produced with a UV-sensitive resin loaded with particles**.** (Liu & Mo, 2010) In addition, the designs of the models can be explicitly customized according to their applications such as tissue and bio-modeling, swimmers, and biomimetics designs. (W. Sun et al., 2005; Wang et al., 2018) The structures built with the additive manufacturing techniques are used in biomedical fields as they are robust, sophisticated, and have multiple dimensions**.**

(Tetsuka & Shin, 2020) Furthermore, the complex structures developed using inkjet and extrusion-based 3D printer techniques have been making progress in medicine with the contribution of biocompatible materials. (Erkoc et al., 2020; Marco, 2015)

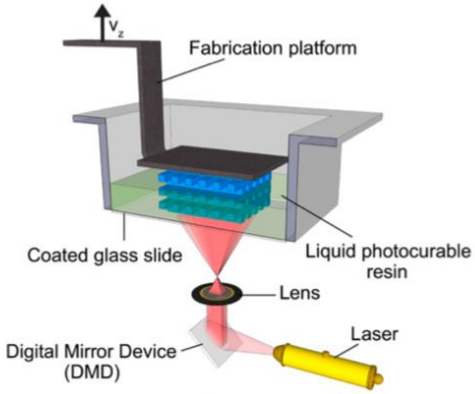

Figure 7 Scheme of Top-Down Stereolithography Setup (Billiet et al., 2012)

2.4 SMALL-SCALE SWIMMERS

The small-scale robots and swimmers are small devices that provide manipulation at the micrometer and nanometer scale, which has been shown to have significant demand, especially the magnetically actuated ones. (Koleoso et al., 2020) These devices can reach hard-to-reach areas due to their miniature size and thus could be assigned in minimally invasive surgery, (Nelson et al., 2010) drug delivery, (Alapan, Bozuyuk, Erkoc, & Sitti, 2020), and biosensing applications. (Sanchez et al., 2011b) The mobility of swimmers and robots is improved by using diverse modalities. Many groups are researching actuation techniques for small-scale mechanisms since these swimmers/robots were utilized efficiently in biological environments to exhibit challenging maneuvers. (Ceylan et al., 2017) One of those, the autonomous propulsion of bio-hybrid micro-swimmers, which are formed by the integration of biological creatures into synthetic structures, can be provided by bacterium species. (Alapan et al., 2018) Another method that provides the actuation mechanism is magnetic induction. It has been argued that providing motion with a magnetic field is more advantageous than other actuation principles; it can be used without manipulating biological areas. (Fischer & Ghosh, 2011) Robots/swimmers that respond quickly to

magnetic field manipulation could be controlled in complex environments. (Fukuda et al., 1994) Considering the swimmer's magnetic torque, propulsion, and hydrodynamic resistance, the hybrid sperm-shaped model and the one side gold and nickel-coated silica Janus microspheres are presented that could swim against the blood flow shown in figure 8. (Alapan et al., 2020; Xu et al., 2020) Furthermore, Hu and colleagues indicated that the soft magnetic millirobot has a wide range of actuation properties such as rolling, walking, and jumping. (Hu et al., 2018)

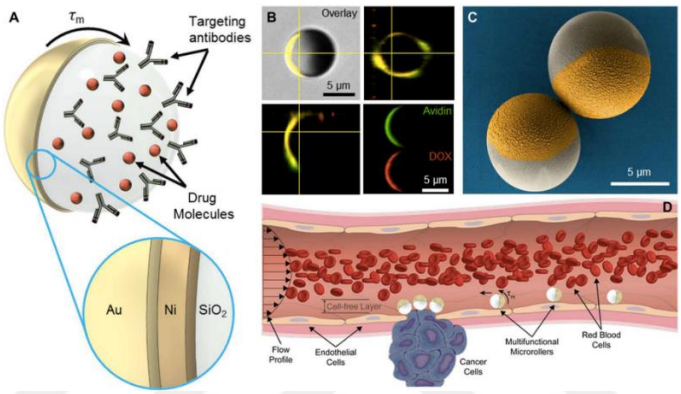

Figure 8 Microscopic Image and Blood Flow Diagram of Au/Ni Coated Silica Micro-rollers
(Alapan et al., 2020)

2.5 MICROFLUIDIC CHANNELS

Microfluidic systems have been used in laboratories during biological research in disposable or non-disposable forms. (Bahadorimehr et al., 2010) The microfluidic channels could be prototyped with a 3D printer in a short time and produced using biocompatible materials. (C. Chen et al., 2016) There are several approaches, such as direct printing and mold-based, in using elastomer materials in the production of microfluidic channels and it has been stated that producing microfluidic channels employing 3D printers can be faster, among other methods. (Mehta & Rath, 2021) Moreover, with this method, inlets, outlets, and valves on the microchannel could be pre-designed and obtained in one-step production. (Mehta & Rath, 2021; Shallan et al., 2014) This hybrid production has also improved the accessible visualization and analysis of the environment by

providing a transparent background. (Alapan et al., 2016) PDMS (polydimethylsiloxane) chemical with a certain amount of a curing agent is poured into the designed molds and cured; this process can obtain channels in various forms. (Villegas et al., 2018) This material is fluid at room temperature, which transforms into a solid elastomer form by cross-linking. (Xia & Whitesides, 1998) Regarding the material itself, in addition to its biocompatibility, its elastic properties make it possible to develop LOC (Lab-on-a-chip) devices, thus providing more design flexibility. (Hongbin et al., 2009; Ozunlu et al., 2021)

2.6 HYPERTHERMIA

The magnetic hyperthermia technique was first introduced in 1957 by injecting iron oxide particles into the tumorous lymphatic tissue of experimental animals. (GILCHRIST et al., 1957) Let's take a closer look at the heat mechanisms of magnetic particles. Eddy current, Brownian, and Neel relaxational and hysteresis losses are the main sources of heat due to magnetic particles under an alternating magnetic field. (Hosseinabadi et al., 2020) However, the eddy current depends on the magnetic field strength and electrical conductivity of the volume of the particles. (Beković and Hamler, 2010; Khursid, 2011) This effect is neglected when considering large surface areas and small-volume nanoparticles. (Khurshid, 2011) Magnetic moments create different relaxation effects in more sparsely and densely dispersed particles under the field. (Périgo et al., 2015) For this reason, heat dissipates by a phenomenon known as hysteresis loss. Particle sizes have been argued as the determining factor in the working principles of these hyperthermia mechanisms. (Kobayashi, 2011) In magnetic hyperthermia relaxation losses at the nano to micrometer-scale particles are associated with Neel and Brownian motions. (Périgo et al., 2012) The heating mechanism of iron oxide particles less than 20 nm is explained by Neel relaxation. (Kobayashi, 2011) It has been stated that particles dispersed in the liquid matrix can generate heat by causing Brownian relaxation due to friction interaction with the medium and movement mechanisms. (Beković & Hamler, 2010)

In this technique, the biological tissues absorb heat, which is induced by the alternating magnetic field, dissipated by the magnetic particles. (Cruz et al., 2017)

The resulting heat triggers structural changes in the tumor cell, first affecting lipids, proteins, and deoxyribonucleic acid, leading to cell death. (Shen et al., 2020) Cancerous cells are either irrevocably damaged or become more susceptible to radiotherapy and chemotherapy simultaneously, depending on the temperatures reached and the duration of treatment. (Jordan et al., 2007) The resulting heat, the frequency of the emitted alternating magnetic field, and the magnetic field strength are determined by the particle type and particle concentration in the target volume. (Beik et al., 2016) Magnetic oxide materials, especially iron oxide, are used in hyperthermia applications by showing superior resistance properties in wide frequency ranges. (Hedayatnasab et al., 2017; Willard & Franco, 2013) For the magnetic field intensity and temperature, it was stated that vast of the cells died after a stage of hyperthermia treatment of Fe_2O_3 nanoparticles at 44°C -to higher temperatures, and the calculated magnetic field (H) value at 400 A (AC) was measured as 335.2 Oe. (Patil et al., 2016) It has been indicated that the healthy cells compared to targeted tumor cells are less damaged with this method. (Khursid, 2011)

2.6.1 SAR (Specific Absorption Rate). The specific absorption rate is the representation of the heating efficiency of solids and liquids under an alternating magnetic field. (Natividad et al., 2008) The specific absorption rate (SAR) is calculated by the equation shown in formula 6, where, C is specific heat, k is constant 4.186 x 10^3 J/cal, $\Delta T/\Delta t$ is the rate of temperature change over time. (Lehmann et al., 1978) Several parameters affect the time-dependent heat exchange of particles, such as saturation magnetization and the size of magnetic particles. (Khurshid et al., 2015) It has been stated that having a shell structure can insulate current loops due to factors such as nano-size distribution and oxide shell in nanoparticles examined by SAR. (Khurshid, 2011)

$$\mathbf{SAR} = \mathrm{k}\,\mathbf{C}\left(\frac{\mathbf{\Delta T}}{\mathbf{\Delta t}}\right)$$

Formula 6. Specific Absorption Rate.

2.7 OBJECT DETECTION

Recently developed object detection algorithms can detect the properties of the objects with the image processing in the traced environment in various applications. (Amit et al., 2020; Raj & Srinivasulu, 2021) These systems have been functionalized to analyze data by collecting color, shape, and velocity. (Rani & Jindal, 2020) Furthermore, tracking and detection algorithms have determined the displacement of the small size particles in their domains. (Barba-Guaman et al., 2017; Gallego-Urrea et al., 2011) Specifically, visualization data has great importance for direct information about the interaction of molecules in the particle integrated biological environment and detected location. (Amit et al., 2020; Stayton et al., 2007)

2.8 SIMULATION

Computational simulation can identify different working possibilities of designs and improve the outcomes gathered from the developed models. Thanks to the algorithm used on small reconfigurable systems, even the living tissues have been simulated to obtain more efficient robots. (Kriegman et al., 2020) Furthermore, the algorithms have been used to model small-scale swimming and robot systems' trajectory movements and drug-delivery mechanisms. (Başağaoğlu et al., 2018; Cregg et al., 2012) Based on the geometric shapes of these small systems, the simulations develop their unique mobility in a liquid environment. The robot/swimmer moving through a liquid medium needs a propulsive force to overcome the fluid dynamic drag. (Fukuda et al., 1994) To create the equation of motion, the forces acting on the mobile robot moving in air-liquid boundary conditions are as follows; (i) fluid drag force and moment, $[F_d; T_d]'$, (ii) fluid buoyancy, F_b, (iii) gravity, F_g, (iv) electromagnetic force and moment, $[F_{em}; T_{em}]'$ and (v) surface tension force, F_c. The equation of motion is described in the below formula. (Arcese et al., 2013)

$$\begin{bmatrix} \mathbf{0} \\ \mathbf{0} \end{bmatrix} = \begin{bmatrix} \boldsymbol{F_d + F_{em} + F_g + F_b + F_c} \\ \boldsymbol{T_d + T_{em}} \end{bmatrix}$$

Formula 7. Equation of Motion.

Stokes's fluid approach uses the fluid drag effect, [Fd; Td], to calculate the force and moment vector. (Berg, 1993) The effect of fluid on motion is calculated by including the diagonal resistance, D. (Johnson & Brokaw, 1979) Fluid effect can be calculated for small-scale swimmers moving across the fluid-air boundary. (Dörr & Hardt, 2015; Eigenbrod & Hardt, 2020) Thus, six degrees of freedom of rigid body motion, [U; Ω], can be related to the fluid forces shown in formula 8.

$$\begin{bmatrix} \boldsymbol{F_d} \\ \boldsymbol{T_d} \end{bmatrix} = \boldsymbol{D} \begin{bmatrix} \boldsymbol{U} \\ \boldsymbol{\Omega} \end{bmatrix}$$

Formula 8. Equation of Fluid Drag.

The forces and moment component can be obtained by the intensity of the 3D magnetic field lines generated by the coils used for the movement control of the swimmers, B, and the magnetic gradient of this field, grad(B). (formula 9) (Beiranvand, 2013) During the acquisition of the components, the measured magnetization vector of the generated robot, m, and the instantaneous projection of the electromagnetic field produced by the coils on the swimmers in motion is represented by the corresponding complex rotation matrix, R. (Spong et al., 2006)

$$\begin{bmatrix} \boldsymbol{F_{em}} \\ \boldsymbol{T_{em}} \end{bmatrix} = \begin{bmatrix} \boldsymbol{m} \cdot \boldsymbol{R grad(B)} \\ \boldsymbol{m} \times (\boldsymbol{RB}) \end{bmatrix}$$

Formula 9. Equation of Force and Moment Components.

To model the solid body, motion, the equation below can be provided by adding gravity and surface tension to the equation. Gravity, F_g, buoyancy, F_b, the sinking volume of the swimmer, V, the density difference of the fluid on which it floats, $\delta\rho$, and the gravity vector, g, can be represented in the same equation. (formula 10)

$$\boldsymbol{F_g} + \boldsymbol{F_b} = \boldsymbol{\delta \rho V R g}$$

Formula 10. Equation of Gravity and Buoyancy.

The surface tension force F_c to be included in the equation can be generated by the last component of the motion. (Smith et al., 1986) For the calculation of the tension force, the tension coefficient σ, created by the wet surface of the robot with the liquid used, and the contact angle, θ, are used as shown in the formula 11. The

perimeter length, l, found in the equation is calculated instantaneously. Direction of application of force k = [0; 0; 1] is determined by the vector.

$$\boldsymbol{F_c = l \cdot \sigma \cdot sin(\theta) \cdot Rk}$$

Formula 11. Equation of Tension Force.

After all forces and moments are integrated, the rigid body motions equation can be calculated as shown below, using the principle of non-accelerated swimming of micro-robots. (Purcell, 1977; Taylor & A, 1951) (formula 12)

$$\begin{bmatrix} \boldsymbol{U} \\ \boldsymbol{\Omega} \end{bmatrix} = -\boldsymbol{D^{-1}} \left(\begin{bmatrix} \boldsymbol{F_{em} + F_g + F_b + F_c} \\ \boldsymbol{T_{em}} \end{bmatrix} \right)$$

Formula 12. Equation of Rigid Body Motion.

CHAPTER 3

MATERIALS AND METHODS

3.1 CHEMICALS

Oleic Acid (%90, Sigma Aldrich, St. Louis, Missouri, United States), $NaBH_4$ (%96, Sigma Aldrich, 71320), Hexane (%96, Sigma Aldrich), Ethanol Absolute (%99, ISOLAB Chemicals), Iron (Fe) powder (%99, Merck, Darmstadt, Germany), Sigma Aldrich, 81280) and $FeCl_2$ (%98, Sigma Aldrich, 372870, St. Louis, MO, USA), Polydimethylsiloxane (PDMS) (Dow Corning Sylgard, Midland), Dimethyl Sulfoxide (DMSO) (%100, OriGen Biomedical GmbH, Germany), distilled (DI) water and Hexane (%96, Sigma Aldrich). ANYCUBIC 3D Printing UV sensitive resin (grey and clear) composed of resin monomers and a photo-initiator) was acquired from Shenzhen (China).

3.2 PARTICLE SYNTHESIS METHODS

3.2.1 Y-Junction Method. The Y-junction tube is a technique that provides a high amount of nanoparticles in short experimental durations. In this project, Fe nanoparticles were synthesized via this method.

3.2.1.1 Fe Nanoparticle Synthesis. The formation of iron nanoparticles occurs by reduction of the iron salt ($FeCl_2$) with $NaBH_4$. $FeCl_2$ and $NaBH_4$ solutions dissolved in distilled water are forced into the Y-shaped tube with the help of the Ar/H_2 gas flow. The two solutions enter a chemical reaction at the junction of the Y tube as shown in figure 9, resulting in the formation of Fe nanoparticles. The nanoparticles were kept in the solution containing hexane. Besides, control of the size of Fe nanoparticles can be achieved by changing the length and inner diameter of the Y-tube. Apart from Oleic Acid (OA), polyethylene glycol (PEG) and/or Oleylamine (Oam) can be used as a surfactant.

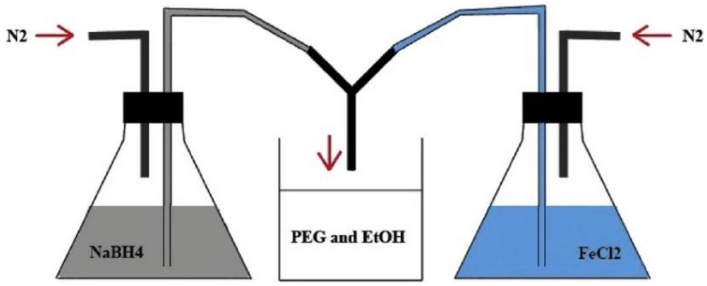

Figure 9 Scheme of Nanoparticle Synthesis System
(Domac et al., 2020)

3.2.2 Ball Milling Method. Ball milling is a mechanochemical method, carried out in a closed mill, to obtain powders of small-sized particles. (figure 10) Milling pure elements or alloys with stainless carbon steel balls in dry or liquid media results in homogenized micro and nano-sized particles. As a result of the friction of particles and balls, the precursor, solvent, and surfactant are ground in the milling jar at certain time intervals.

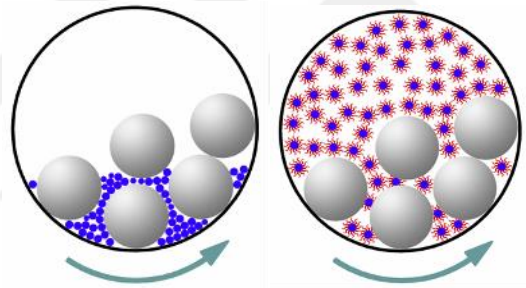

Figure 10 (left) Classical and (right) Surfactant-assisted Ball Milling Schematics
(Akdogan, Hadjipanayis and Sellmyer, 2009b)

3.2.2.1 Fe Flakes Synthesis. 10 µm Fe powder with irregular shape was milled by MTI Corporation SFM-1 planetary ball mill system. The 10:1 ratio was chosen for the iron powder and stainless-steel ball, respectively. Milling was performed in a steel flask at a rotational speed of 700 rpm for 12 hours with the addition of hexane and oleic acid, which are dispersant and surfactant, respectively. At the end of the experiment, the thickness of the Fe flake was measured to be between 100-200 nm using Scanning Electron Microscope (SEM). The Fe flakes were cleaned by sonication in ethanol followed by centrifugation; the procedure was repeated four times and the as-prepared flakes were kept in %96 Hexane.

3.2.2.2 Nd-Fe-B Flakes Synthesis. Nd-Fe-B flakes were synthesized by the surfactant-assisted ball milling technique using a planetary ball mill (MTI Corporation SFM-1) with stainless steel balls. The powder to weight ratio of the ball was 10:1, and heptane and oleic acid were used as dispersant and surfactant, respectively. The mixture was ball milled at 700 rpm for 12 hours. The micro flakes were cleaned by centrifugation in ethanol, the supernatant was removed, and the particles were stored in %96 Hexane.

3.3 PREPARATION OF 3D PRINTED MILLISWIMMERS

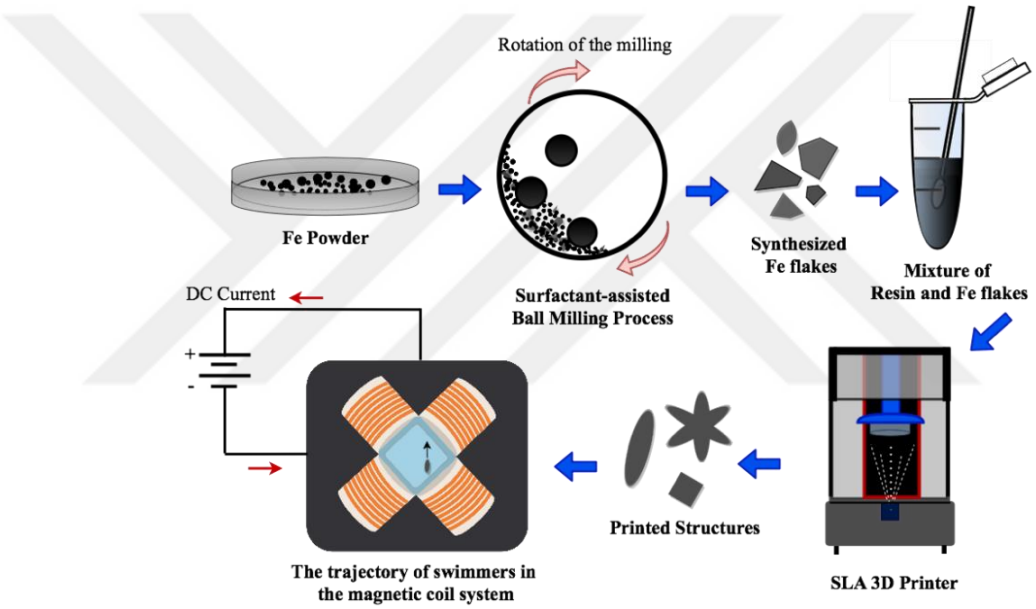

Figure 11 Schematic of the Synthesis of Magnetic Milli-swimmers (Hira Domac et al., 2021)

The various steps that were followed to obtain a magneto-sensitive milli-swimmer are shown in figure 11. Synthesized magnetic particles have been integrated into 3D printed swimmers since they have restricted mobility on their own and are challenging to control. The 3D models of swimmers were designed by using Computer-Aided Design (CAD) software. The swimmer and prototypes were printed using an SLA-based Anycubic Photon 3D printer with a light source of 405 nm shown in figure 12. UV sensitive resin was used as the main material of the swimmers, which were modeled layer by layer with the photochemical process.

All structures were printed using 405 nm light-sensitive Anycubic polymer resin material (ingredients not disclosed due to trade reasons of the respected company) includes resin monomers and photocuring agent. The xy-resolution value of the printer is 47 microns. The selected layer thickness and the estimated total print volume are 100 microns and 0.01 ml for each swimmer, respectively. The overall print time was approximately six minutes for each swimmer.

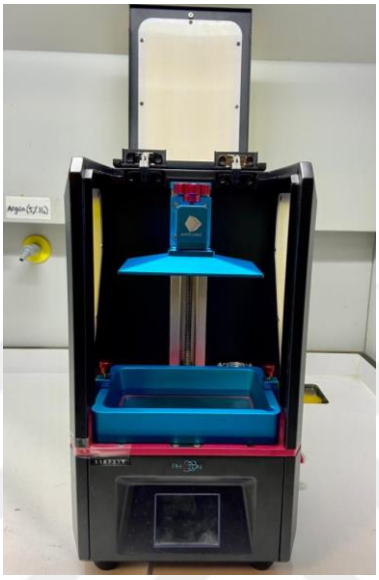

Figure 12 Anycubic Photon 3D Printer

Milli and sub-milli swimmers were designed with CAD software and saved in standard triangle language (STL) format. It became ready to print by using the user interface/control software to print the structures. (figure 13)

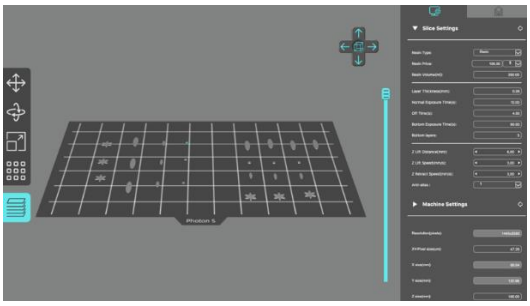

Figure 13 Interface of 3D Slicer Software

The particles with ferromagnetic properties were mixed with the photocurable polymeric resin, which is the primary material of the produced sub-milli and milli-swimmers which are Nd-Fe-B, Fe flakes, and Fe nanoparticles.

A 0.5% wt/vol concentration was obtained by mixing 0.2 g of magnetic particles and 40 ml of polymer resin for each magnetic particle-resin combination. Before beginning the printing process, the mixture was sonicated for 30 minutes to prevent the magnetic particles from being aggregated. The resulting mixture was transferred to the tank, and the build platform was settled to print the structures. After the printing process, the swimmers were cleaned with 99% pure ethanol for 3 minutes as cleaned unpolymerized resin. To make them more permanent and rigged, the photocuring process of the swimmers was continued by exposing them to the 395 nm wavelength of the excitation UV light was for 25 minutes.

3.4 CHANNEL DESIGN

The '+' shaped resin-made channel designed with a CAD program was printed by a commercial printer, Anycubic Photon S. (Figure 14) The 405nm Anycubic photosensitive transparent resin was used for providing a transparent framework. The direct printing method was used for this channel, and the experiment duration was 1 hour. The length of the channel was designed as 2.4 cm and 0.8 cm. After fabrication, the channel was cleaned with pure ethanol for 3 minutes. In a second manufacturing technique, a mold was produced using a 3D printer.

The mold of the PDMS channel was designed following the dimensions of the electromagnetic system. The long and short edges of the channel mold were designed as 2.2 cm and 0.7 cm, respectively. (Figure 14) Polydimethylsiloxane (PDMS) was prepared by mixing the prepolymer and curing agent in weight ratios of 10:2 and poured into this mold. Then it was left to dry for about two days. Thus, the functional channels are obtained according to the dimension of the swimmers.

The back and front sides of the duct were attached with adhesive.

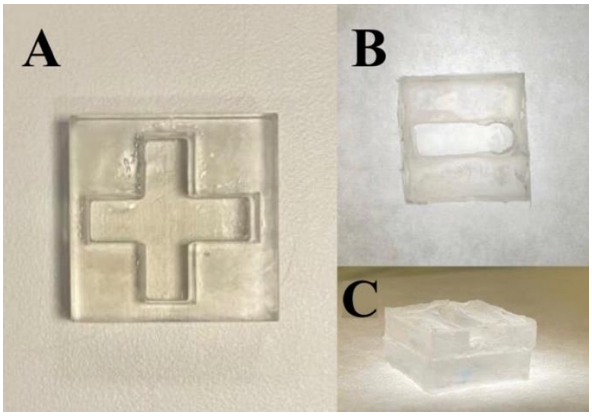

Figure 14 (A) Direct Printing Polymer Resin Channel. PDMS-based (B) and (C) Line-shaped Channel

3.5 ELECTROMAGNETIC SYSTEM

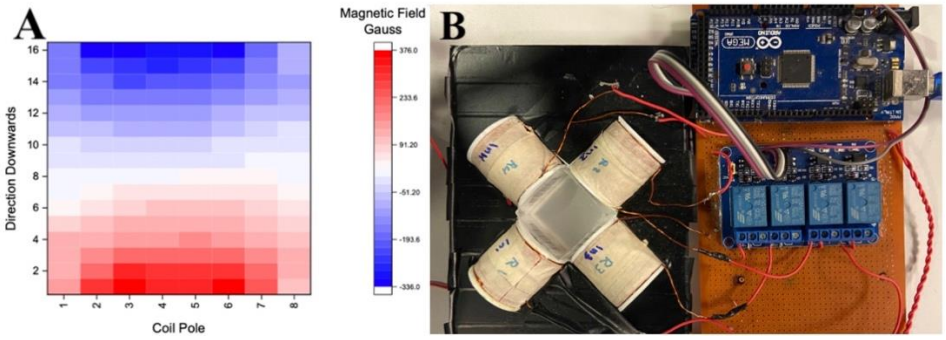

Figure 15 Magnetic Field Maps and (B) Electromagnetic Control System (Alshammari et al., 2021)

Examination of the magnetic activity of the milli and sub-milli swimmers was performed using an electromagnetic coil system, which consists of four coils as shown in figure 15. Each coil was controlled with a four-channel relay component and Arduino microcontroller. The movement trajectories of the swimmers were guided manually using the digital interface. The magnetic field gradient map provides a maximum value of 376 Gauss for a current value of 2 amperes. (figure 15) For the specifics of the homemade electromagnetic setup, please refer to the work by Al-Shammari et. al. (Al-Shammari et al., 2021)

3.6 PARTICLE PREPARATION FOR HYPERTHERMIA

For the magnetic hyperthermia process, synthesized magnetic particles and solutions were prepared with various concentrations. Resin, PDMS, and agar gel-particle solution concentrations were obtained by mixing with the particles. The particle-liquid concentration was prepared in glass test vials. The solution was sonicated and vortexed for 5 minutes to increase the settling duration of the particles in the liquid. Particle resin solution kept at room temperature.

3.7 SWIMMER DETECTION SYSTEM

Various systems were operated together to detect the position of swimmers in a confined area. NVIDIA Jetson Nano developer kit with Linux operating system was used to run the image processing algorithm. The algorithm is written with the Python programming language and the OpenCV (Open-Source Computer Vision Library) library for GPU (graphics processing unit) modules. The Raspberry Pi Camera v2.1 (8 megapixels) module is connected to the development board fixed with a tripod, observed the experimental area from a height of three centimeters, shown in figure 16. The algorithm that enables the electromagnetic system to operate over the interface is shown in figure 17. The coils were operated with the DC power supply, while the developer kit was supplied power to the electromagnetic relay modules and camera.

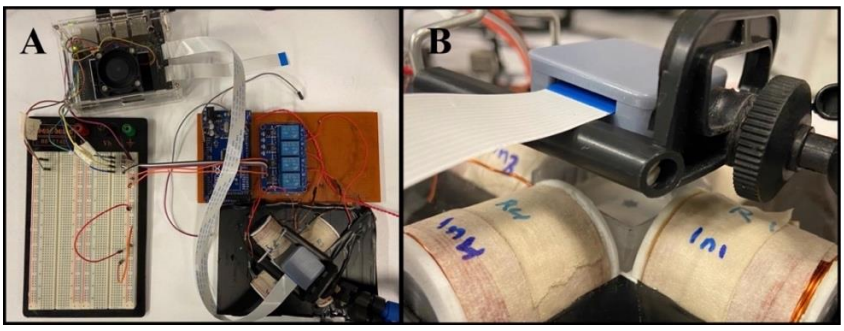

Figure 16 (A) Real-Time Detection/Control System and (B) Experimental Area

```
33
34  cv2.namedWindow('Trackbars')
35  cv2.moveWindow('Trackbars',1100,0)
36
37  cv2.createTrackbar('hueLower' , 'Trackbars', 0,179 , nothing)
38  cv2.createTrackbar('hueHigher', 'Trackbars', 100,179, nothing)
39  cv2.createTrackbar('hue2Lower' , 'Trackbars', 0,179 , nothing)
40  cv2.createTrackbar('hue2Higher', 'Trackbars', 179,179, nothing)
41  cv2.createTrackbar('satLower' , 'Trackbars', 0,255, nothing)
42  cv2.createTrackbar('satHigher', 'Trackbars', 255,255, nothing)
43  cv2.createTrackbar('valLower' , 'Trackbars', 0,255, nothing)
44  cv2.createTrackbar('valHigher', 'Trackbars', 104,255, nothing)
45  cv2.createTrackbar('ParticleX','Trackbars',200,600,nothing)
46  cv2.createTrackbar('ParticleY','Trackbars',150,450,nothing)
47
```

Figure 17 Snapshot of Trackbar Interface Code

3.8 CHARACTERIZATIONS

3.8.1 Magnetic Characterization. The magnetic properties of the swimmers and particles were measured by vibrating sample magnetometer (VSM) Dexing Magnet VSM 550 and Quantum Design PPMS in Sabancı University and Dokuz Eylül University, Center for Fabrication of Electronic Materials. The samples were dried on the flask and were analyzed at room temperature.

3.8.2 Structural Characterization. The nano and microparticle composition and morphologies were characterized by scanning electron microscope (SEM) Leo SUPRA 35VP FEG-SEM. X-ray diffractometer (XRD) for the particles crystallographic structures and chemical compositions were analyzed by Bruker D2 Phaser in Sabancı University (EFSUN). The swimmer morphologies were performed by OPTIKA (B-383LD) Fluorescence light microscope (figure 18).

Figure 18 OPTIKA Light Microscope

3.8.3 Induction Heater. An induction heating device developed during this study (MSG Electric) was used for the magnetic hyperthermia studies at 5 Oesterd. During the experiment, the glass vial was centrally set in the induction coil (ZVS, 12-48V 20 A 1000W). The coil was made of 4 cm inner diameter, 5.8 cm length, and 7 turns, shown in figure 19. The releasing heat from the particle-liquid concentration while hyperthermia experiments were measured by an infrared (IR) temperature sensor. (DFRobot, TS01 Non-contact IR Temperature Sensor) The magnetic field was measured with a tesla meter (PHYWE, 136010-93). (Figure 20)

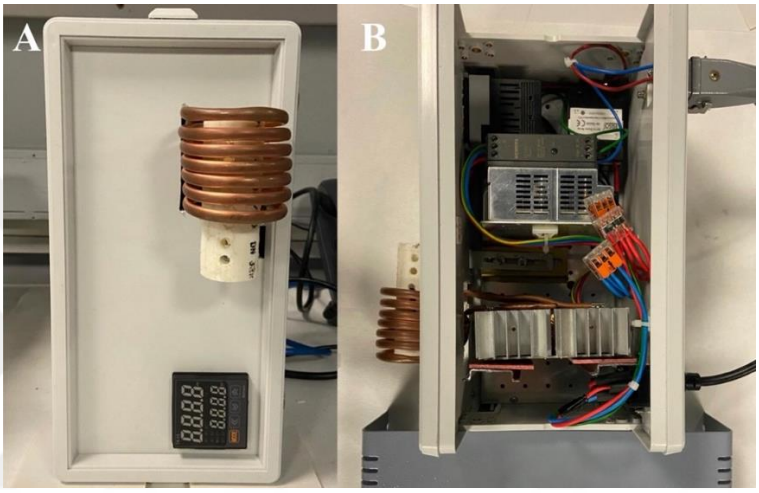

Figure 19 (A) Induction Heater Device and (B) Internal Part of the Device

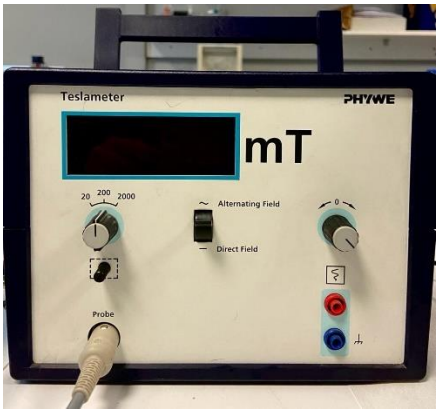

Figure 20 Teslameter for Magnetic Field Measurement

CHAPTER 4

RESULTS AND DISCUSSIONS

4.1 MAGNETIC MATERIALS

4.1.1 Fe Nanoparticles. SEM images of Fe nanoparticles reveal spherical morphology (figure 21). Transmission electron microscope (TEM) images result shows an average particle size of 92nm. XRD analysis of Fe nanoparticles are indexed to BCC α-Fe phase (figure 22) Magnetic characterization of nanoparticles reveals low magnetization and coercivity at room temperature. (figure 23)

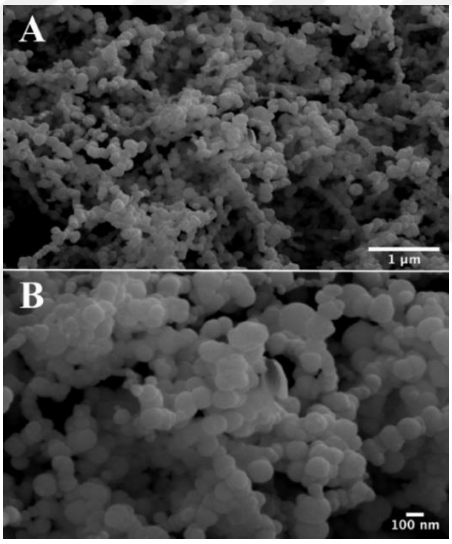

Figure 21 (A) SEM Images of Fe Nanoparticles

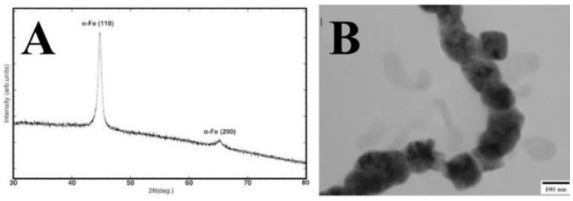

Figure 22 (A) X-ray Diffraction Analysis and (B) TEM Images of Fe Nanoparticles

(Ozunlu et al., 2021)

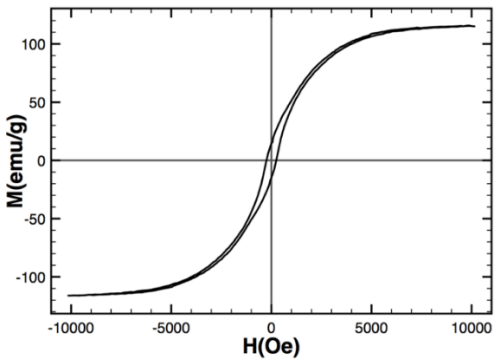

Figure 23 Hysteresis Loop of Fe Nanoparticles

4.1.1.1 Fe/Fe_3O_4 Nanoparticles on Cancer Treatment. The use of Fe/Fe_3O_4 nanoparticles in the medical field are long known to be approved by FDA and is discussed in **2.1.1.** section. The cancer treatment ability of the Fe/Fe_3O_4 nanoparticles was also assessed. The Fe/Fe_3O_4 nanoparticles (13 and 21 nm) have been synthesized using the Y-junction technique. (Domac et al., 2020) According to XRD, the results of the nanoparticles are indexed to α-Fe and Fe_3O_4 phases. (Domac et al., 2020) (figure 24) Magnetic properties of Fe/Fe_3O_4 nanoparticles have revealed 350 Oe coercivity. (figure 24) (Domac et al., 2020) (figure 25) The effects of polyethylene glycol (PEG) coated Fe/Fe_3O_4 nanoparticles were investigated on NIH3T3 (healthy fibroblast) and A549 (lung cancer) cells. (Domac et al., 2020) The viability tests (IC50) were performed with different concentrations of nanoparticles on NIH3T3 and A549 cells in vitro. (Figure 24) It has been observed that nanoparticles have toxic effects on cancerous cells compared to healthy cells. (Domac et al., 2020) (figure 24) Furthermore, the cell viability IC(50) was also tested by Paclitaxel drug on the same cancer cell line. (Domac et al., 2020) (figure 26) Thus, the results demonstrated that nanoparticles at low concentrations (1 μg/ml) have more toxic effects than those of the specific cancer drug concentration (11.1 μg/ml). (Domac et al., 2020)

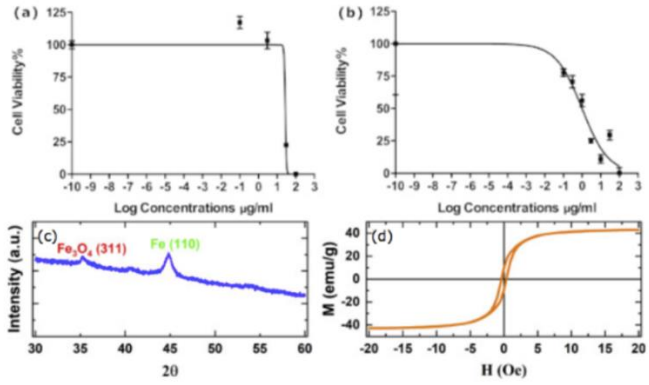

Figure 24 Cell Viability Results of Nanoparticles at Different Concentrations (IC50) (a) NIH3T3 Cells, (b) A549 Cells, (c) XRD and (d) VSM Results

(Domac et al., 2020)

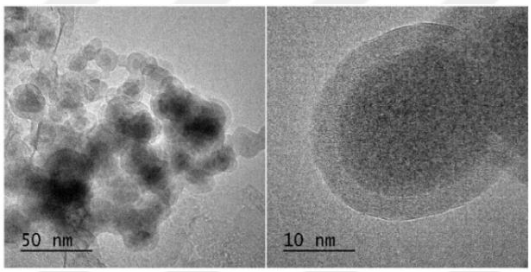

Figure 25 TEM Images of the Fe_3O_4 Nanoparticles

(Domac et al., 2020)

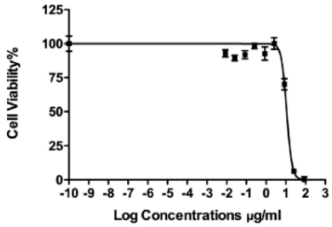

Figure 26 Viability vs. Concentration on A549 Cancer Cell Graphs

(Domac et al., 2020)

Nanoparticles have been revealed to have a 100 times higher toxicity effect on A549 cells compared to previous studies. (Domac et al., 2020; Malvindi et al., 2014; Watanabe et al., 2013) It has been postulated that the toxic effects of the particles have been caused by the iron ions (Fenton reaction) released by the Fe core. As a result of this novel study, it has been proven that PEG-coated Fe_3O_4 nanoparticles can be used as an anti-cancer drug. (Domac et al., 2020)

4.1.2 Fe flakes. The scanning electron microscope (SEM) images show a a shift from an irregular shape to a flake morphology with an ultra-high-aspect ratio (100 nm thickness and 10 μm lateral length). (figure 27) The X-ray diffraction patterns of the precursor powder and as-prepared flakes were indexed to α-Fe body-centered cubic (BCC) crystalline structure. (figure 27) The magnetic hysteresis curves for both the initial Fe powder and flake sample shows that the Fe flakes have a low coercive force and a high magnetization, indicating a soft ferromagnetic response. (Figure 27)

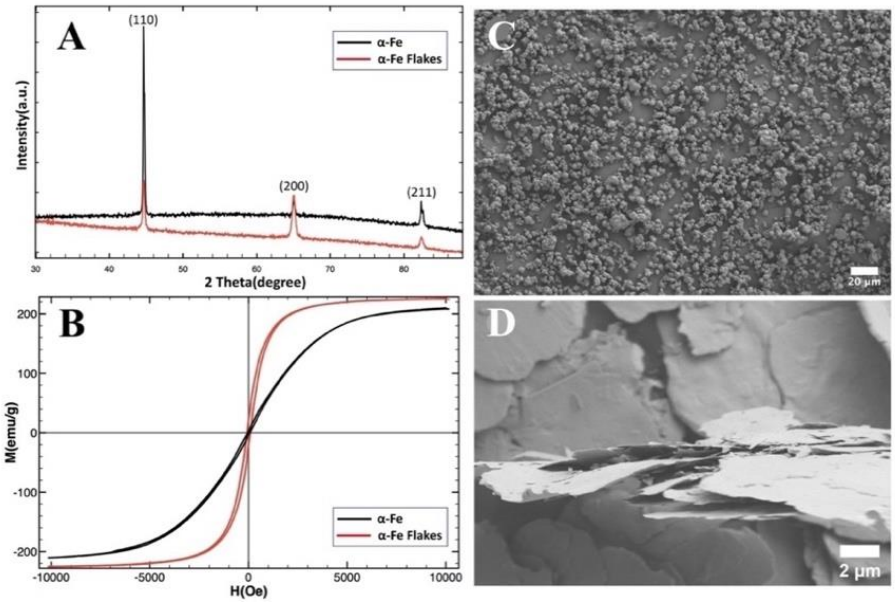

Figure 27 (A) XRD and (B) VSM Results, (C, D) SEM Images of the Fe Flakes

(Hira Domac et al., 2021)

4.1.3 NdFeB flakes. SEM image indicates the morphology of Nd-Fe-B particles. (figure 28) XRD data is indexed to $Nd_2Fe_{14}B$ FCT structure. The magnetic hysteresis loop analysis for the Nd-Fe-B microparticle sample shows ferromagnetic behavior at room temperature. (figure 28)

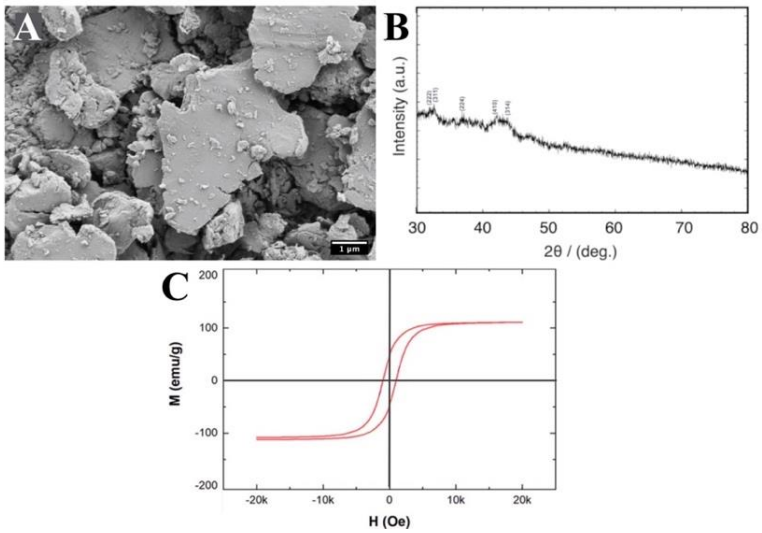

Figure 28 (A) SEM image, (B) XRD and (C) VSM Results of Nd-Fe-B Flakes

(Ozunlu et al 2021)

4.2 3D PRINTED MAGNETIC SWIMMERS

The structures were obtained because of the hardening of the photosensitive resin with the photopolymerization reaction. The experimental studies of 3D-printed ellipsoidal, flower, and square-shaped swimmers (figure 29), which are in locomotion under the influence of magnetic field gradient, have revealed that they create unique trajectories depending on weight and morphology variations. The structural dimensions of the swimmers are shown in table 2.

Figure 29 Fabricated Magnetic Swimmers, Size Comparison with the Coin

Table 1

Properties of milli and sub-milli-swimmers.

Structures	Body length	Shortest length	Thickness (thick and thin)	Weight (thick and thin)
Ship 1	7 mm	2 mm	1mm / 0.2mm	22mg/2.9mg
Ship 2	3.5 mm	1 mm	1mm / 0.2mm	5.9mg/0.75mg
Flower	5 mm	1.1 mm	1mm / 0.2mm	12.5mg/2.2mg
Square	1 mm	0.8 mm	0.8mm / 0.2mm	1mg/0.35mg

The magnetic material distribution in the magnetic swimmers was studied and analyzed with a light microscope (Optica/B-383LD). The embedded magnetic particles dispersion in the swimmers was demonstrated to be random. (figure 30) It is observed that the swimmers have unstable colloid properties. However, due to the interparticle potential, the aggregated magnetic particle distribution may be related to the magnetostatic forces and the viscous nature of the resin matrix. (Puisto et al., 2012) It has been discussed that the particle dispersion in the resin matrix can block UV light and inhibit the photocuring process of the material. (Weng et al., 2016) However, two different resin-particle concentrations were synthesized (%0.5 and %1 wt/vol), shown in figure 30. It has also been stated that the magnetic particles added to the resin and the viscosity of the resin are directly proportional. (Liu and Mo, 2010) Therefore, the lower the viscosity of the resin, the better the dispersion of the magnetic particles in the resin. For this reason, 0.5% wt/vol concentration was chosen instead of the higher concentrations for the resin particle ratio.

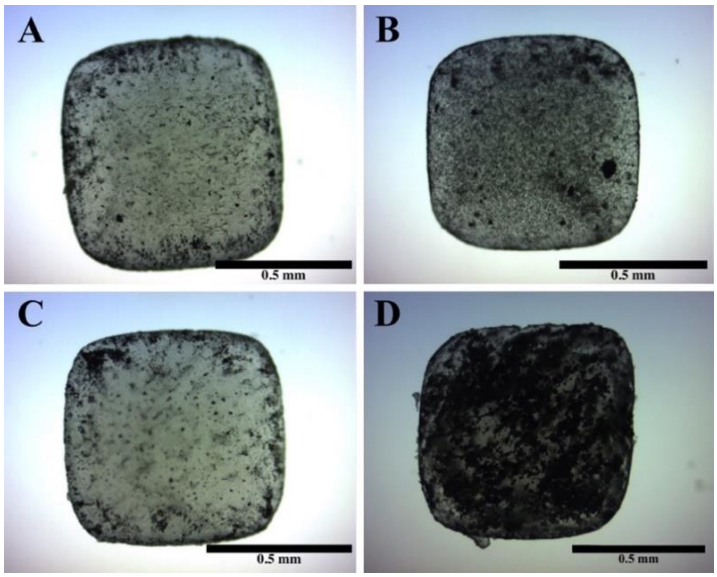

Figure 30 Square-shaped Swimmers with %0.5 wt/vol (A) Fe Flakes, (B) Fe Nanoparticles, (C) Nd-Fe-B Flakes, and (D) %1 wt/vol Fe Flake-based Swimmer

In figure 31, the hysteresis loops at the room temperature of the magnetic milli-swimmers revealed that Fe flakes and resin-based swimmers possess magnetic behavior, although Fe nanoparticles and Nd-Fe-B flake-based swimmer exhibited hard magnetic behavior.

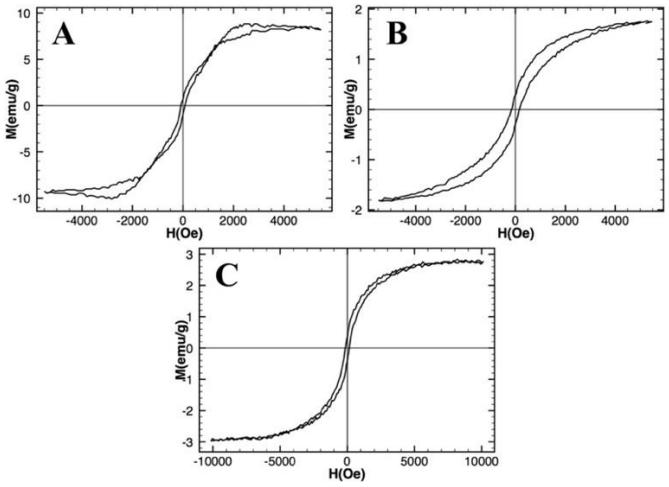

Figure 31 Hysteresis Loops of (A) Fe flake/resin, (B) Nd-Fe-B/resin, and (C) Fe Nanoparticle/resin-based Ship2

The present study determined experimental and theoretical velocities by the drag force and magnetic field gradient acting on the elliptical, star, and square-shaped swimmers moving in distilled (DI) water. The swimming performance of

the milli-dimension structures was investigated using a four-coil electromagnetic control system under a magnetic field gradient. Milli-swimmers were properly tracked using ImageJ, (Rueden et al., 2017) a tracking tool, and experimental speeds were calculated with Chemotaxis & Migration Tool open-access software. (Yan et al., 2020) (figure 32) The experimental velocities of Nd-Fe-B, Fe flake, and Fe nanoparticle-based swimmers' speed comparison graphs are shown in figure 33. The impacts of magnetic particles used in the synthesis of swimmers on actuation and trajectory performances are discussed below.

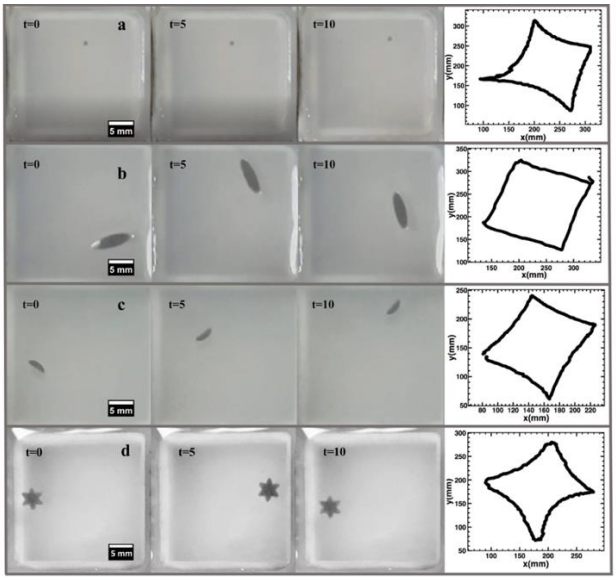

Figure 32 Snapshot and Trajectories of the Fe flake-based Swimmers (Hira Domac et al., 2021)

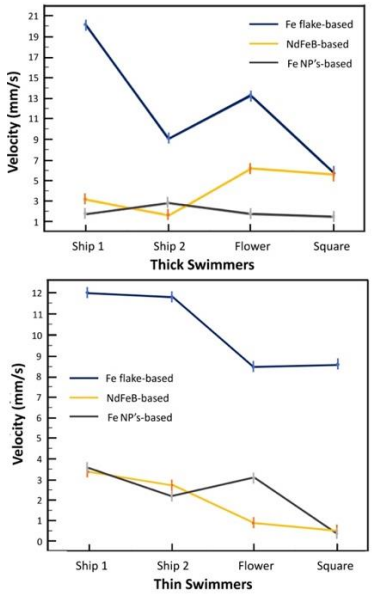

Figure 33 Speed Comparison of the Different Thickness (A) 1mm and (B) 0.2mm

The ellipsoid-shaped swimmers that have been analyzed can be more advantageous in cargo transports and capturing than spherical swimmers due to their asymmetric and large surface area. (Kirvin et al., 2021) In addition, an elliptical winged robot is presented due to the advantage of increasing drag force in a liquid medium. (Yesin et al., 2006) The speed of swimmers conjugated with Fe flake was by far higher than that of equivalents. This crucial reason can be explained due to the Fe micro flakes have high magnetization values with a large surface area and anisotropic texture. (Skomski & Sellmyer, 2009; Zirhli et al., 2020)

In this study, the theoretical speeds were calculated according to the drag force equation. (Formula 4) The 3D printed magnetically responsive milli-swimmers speeds in liquid medium (DI water) were calculated theoretically as 13.54 mm/s, 9.9 mm/s, 10 mm/s, and 8.98 mm/s for milli ship1, milli ship 2, sub-mm square, and milli flower, respectively. The drag coefficient C_d values are used for the elliptic, square, and cube-shaped swimmers were taken as 0.045 (airfoil) and 1.05 (cube), respectively. (formula 5) The drag coefficients were chosen according to the swimmer's geometries. The swimmer theoretical velocities calculated according to using this coefficient are shown in table 3.

Table 3

The drag coefficients and theoretical velocities

Structures	Drag coefficient	Velocity
Ship 1	0.045	3.1 mm/s
Ship 2	0.045	2.4 mm/s
Square (1mm)	1.05	3.7 mm/s
Square (0.8 mm)	1.05	4.7 mm/s

The differences between theoretical and experimental velocities can be explained by the relationship between magnetic particles and magnetic field, although they have the same morphology and thickness characteristics. As mentioned above, during the 3D printing process, the distribution of magnetic particles in the swimmers is entirely random. (figure 30) Due to the particle

aggregation that may occur, the trajectory movements of the swimmers in the magnetic field change as shown in figure 34. Due to local particle aggregation in Fe flake-based Ship1 swimmer, its resulting trajectory differs from the paths shown in Figure 32, which may be due to the particle aggregation shown in the figure 34. The speed of this swimmer was experimentally observed as 42.4 mm/s.

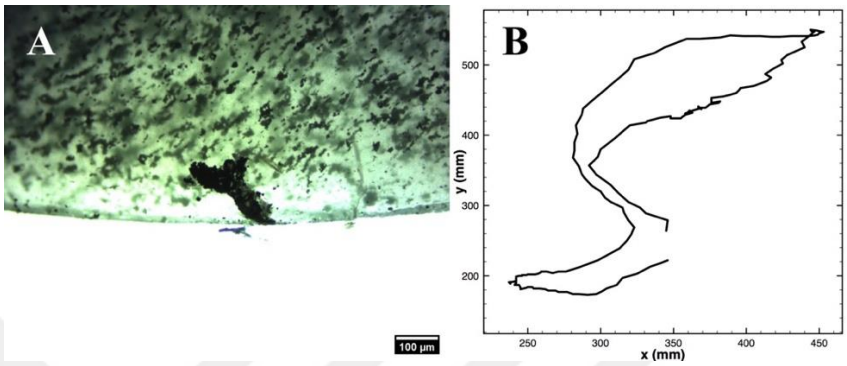

Figure 34 (A) Particle Aggregation and (B) the Trajectory of the Ship1

In this study, it was observed that the thick elliptical Ship1 milli-swimmer has a bigger surface area than the other structures, thus actuating faster because of their response to the magnetic field gradient. Furthermore, it has been examined that, thicker swimmers actuate faster than thin structured swimmers under the same magnetic field gradient. The reason for this increase is the concentration of magnetic particles in the swimmer can also increase the speed of the swimmers. Due to the swimmers' velocity being proportional to the total volume of the magnetic particles, it is emphasized that it could become more sensitive under the magnetic field gradient. (K. S. Kim & Park, 2005)

Consequently, many swimmers and robots with complex movement mechanisms have been presented to the literature. (Ahn et al., 2019; X. Z. Chen et al., 2018; Lu et al., 2018; Palagi et al., 2019) However, these samples are conjugated with ready-made magnetic particles, and the control mechanism on these particles is limited. (Alapan, Bozuyuk, Erkoc, Karacakol, et al., 2020; Hu et al., 2018; Lu et al., 2018; Zhu et al., 2015) Another deficiency, the rapid design, manufacture, and testing of swimmers require lower-cost equipment. In order for these systems to be used for diagnosis and treatment in the medical field, low-budget facilities should be available to patients. (Beg et al., 2020)

4.3 CHANNELS

Channel and molds for milli-swimmers were produced using a 3d printer. These channels are produced according to the dimensions of the electromagnetic coil system. Channels are cleaned and reused after the experiments.

It is seen that the swimmer can easily move under the magnetic field gradient in the channel by using transparent polymer resin in the DMSO medium. (figure 35) The flower-shaped swimmer was also observed in the PDMS-based channel. (Figure 36) Reusable fluidic channels have been a crucial step towards drug delivery and lab-on-a-chip mechanisms. (Anderson et al., 2013)

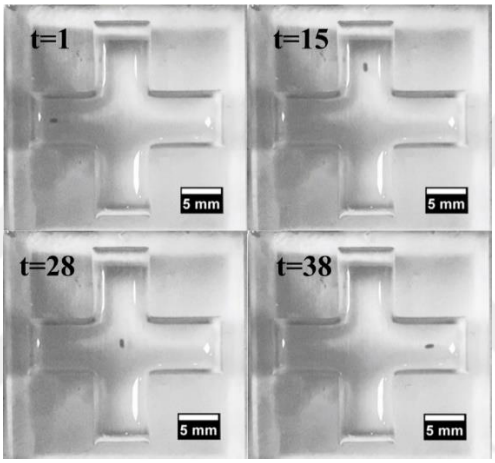

Figure 35 Time-dependent Position (The time unit is seconds)

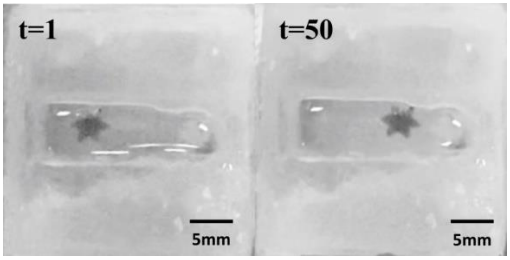

Figure 36 PDMS Channel (The time unit is seconds)

4.3.1 Issues with PDMS-based Channels. PDMS prepared at a ratio of 10:1 was poured into the molds produced with a 3D printer. The PDMS mixture did not dry in the mold for one week. Since the PDMS mixture did not dry in the mold for a week, the other option was epoxy resin, which dried quickly after pouring into a 3d printing mold. The problem here was that the dried epoxy resin was completely stuck to the mold and could not be removed. It was

observed that the printed mold was deformed. Deformation of structures can be prevented by using more rigid and reinforced glass resin for 3d mold designs. For this reason, the ratio of prepolymer curing agent was increased to 10:2 to obtain a rigid PDMS mixture. The channels dried in the mold within two days. As a result, the channel was properly removed from the mold and formed into a channel, as shown in figure 14. Swimmers have been successfully actuated in this channel. (Figure 36)

4.4 CALORIMETRIC MEASUREMENTS

The magnetic particles' local heating effect was performed using an alternating magnetic field. The time versus temperature effect of magnetic micro and nanoparticles was evaluated at a 3.9 kA/m magnetic field (5 Gauss) using the magnetic hyperthermia setup. The alternating current is induced by the magnetic field. Samples were placed inside the helical-shaped induction coil. A cooling fan was used to prevent the work coil from overheating during the experiment. The temperature was observed by a thermocouple located 4 cm from the tubes, and data were collected manually. Figure 37 displays the temperature versus time graphs resulting from the heat dissipated by the particles locally. The hyperthermia experiments were repeated three times for each particle and concentration value. The test solution was sonicated for each experiment.

The particles in the resin medium and three different concentrations were prepared for each three different magnetic particles (Nd-Fe-B, Fe flakes, and Fe nanoparticles). It has been observed that as the magnetic particle density is increased, the amount of heat produced by the samples over experiment time increases.

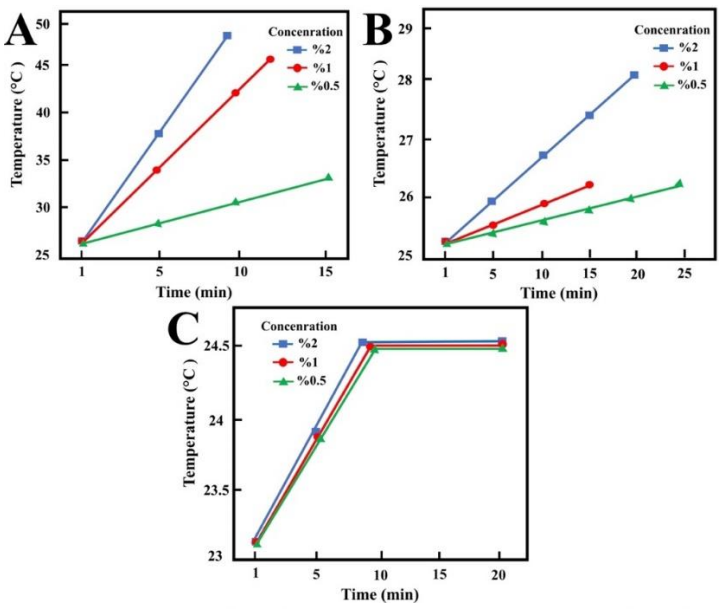

Figure 37 Time vs. Temperature Curves of (A) Fe Flakes, (B) Fe Nanoparticles, and (C) Nd-Fe-B Flakes in the Resin Medium

The heat mechanisms that magnetic particles exhibit in their environment are related to media viscosity, particles volume/size, and magnetic anisotropy in induction heating. The localized heat effect of the 93nm Fe nanoparticles and Fe flakes (100 nm thickness and 10 μm lateral length) can be explained by Brownian relaxation. Here, the localized heat released by the 2% w/v concentration of the Fe flakes solution reached 45°C, almost twice as quickly as the sample prepared with 1% wt/vol concentration. (figure 37) The test solution prepared with %2 wt/vol Fe nanoparticles could reach a maximum temperature of 28 °C in 20 minutes. On the other hand, Nd-Fe-B microparticles could not release heat in the alternating magnetic field. It is shown that the hyperthermia mechanisms of the particles depend on the properties of the magnetic materials, such as saturation magnetization and anisotropy values.

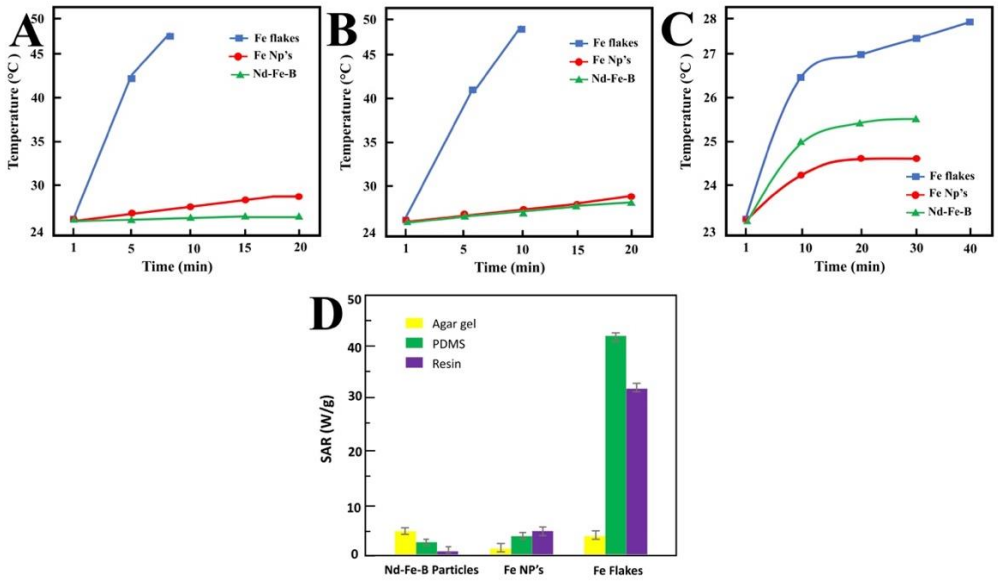

Figure 38 Time vs. Temperature Graphs of %2 wt/vol Concentrations (A)Resin, (B) PDMS, (C) Agar Gel and (D) SAR Values

Three different liquids with different heat capacities were chosen for calorimetric measurements, and the heat dissipation effects of the particles were observed. It was observed that the specific absorption efficiency of Fe flakes was more effective for each liquid medium than the Fe nanoparticles and Nd-Fe-B microparticles. Besides, it has been argued that the ferromagnetic behavior and the anisotropic nature of Fe flakes have a high potential for hyperthermia applications regarding thermal efficiency. (Avolio et al., 2019; Coïsson et al., 2017) Especially, in the resin and PDMS mediums, Fe flakes dissipated heat faster and in a short time. (figure 38) On the other hand, the heat mechanisms of the magnetic particles in the agar gel medium are associated with hysteresis loss. The reason why the particles in this solution emit lower heat can be associated with the inability of the particles to rotate and vibrate as a result of high viscosity, and the insufficient frequency of the induction heater used.

4.5 DETECTION SYSTEMS

4.5.1 Video Recording Detection. Object detection algorithm was implemented using MATLAB 2019b to track swimmers with the video source. An algorithm has been developed using blob analysis to detect the regions that change in the image in terms of brightness and color characteristics. (figure 39) More detailed code information is given under the appendix section **A. Trajectory Code (Video Source)**. The shape inserter feature in the Computer Vision System Toolbox was used to detect the darker (dark gray) swimmer on the background with white and gray tones. (figure 39) The position data processed according to the trajectory of the swimmer is detected and shown in the plot. (figure 40) In order to activate the real-time object tracking algorithm studies were carried out with the Raspberry Pi 3 Model B operating system and Raspberry Pi Camera Rev 1.3 camera. However, some limitations occurred during the data processing of this algorithm via live image. It captured more than one point due to the tonal differences caused by the reflection of the light from the water in the experimental area watched by the camera. For this reason, this algorithm was limited to the object tracking feature from the video.

```
detector = vision.ForegroundDetector(...
       'NumTrainingFrames', 5, ...
       'InitialVariance', 30*30);

blob = vision.BlobAnalysis(...
       'CentroidOutputPort', false, 'AreaOutputPort', false, ...
       'BoundingBoxOutputPort', true, ...
       'MinimumBlobAreaSource', 'Property', 'MinimumBlobArea', MAB);

shapeInserter = vision.ShapeInserter('BorderColor','White');

videoPlayer = vision.VideoPlayer();
```

Figure 39 Snapshot of the Detection Code

Although information about trajectory motion plot is obtained, there are certain restrictions on image processing over video. Hereof, it was considered appropriate to use a live feed object tracking algorithm.

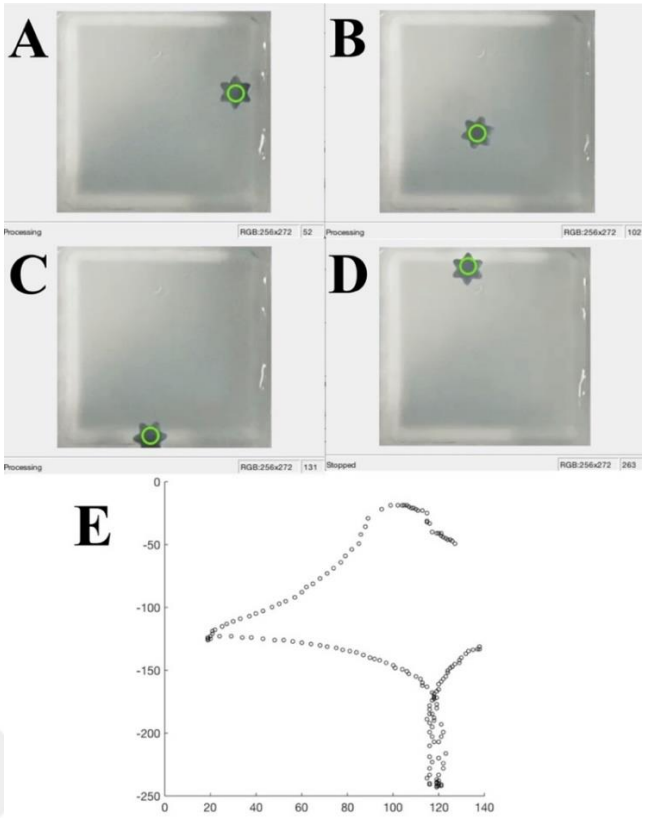

Figure 40 Snapshots of the Swimmer Movement with Various Frames at (A) 52, (B) 102, (C) 131, (D) 263, and (E) Trajectory of Flower

4.5.2 Real-Time Detection. A trajectory algorithm was implemented with coordinates of the object's center of mass on the detected image from the live feed. The swimmer in a frame is spotted during target detection.

By changing the contrast value, the swimmer is detected in the black and white filtered vision. (figure 41) The position data of the swimmer in the area monitored by the camera (640x480) is shown in figure 16. The location data of the milli-swimmer indicated the instantaneous and desired positions blue and red fonts, respectively. The swimmer's position uses the live tracking feedback system to enable the coils to be opened and closed sequentially. Thus, the swimmer could travel to the XY axis targeted area using the trackbar interface (ParticleX and ParticleY). The electromagnetic and the live feedback system with the camera were developed more effectively through a code to track the swimmer. The code is provided under appendix section **B. Real-time Swimmer Detection Code.**

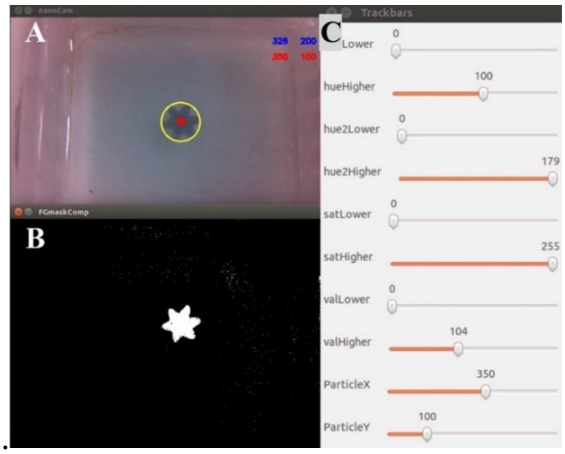

Figure 41 Snapshots of the (A) Tracked Area, (B) Masked Image of Swimmer and (C) Trackbar

4.6 SIMULATION

The linear equation system was computed numerically by using Ordinary Differential Equation (ODE) solution in MATLAB and SIMULINK (2019b & v12) environment. A simulation has been developed to improve results compatible with experimental measurements by calculating the movement of swimmers in the magnetic field and the forces that act on the swimmer. The simulation is done over the force balance on the y-axis, as shown in figure 42.

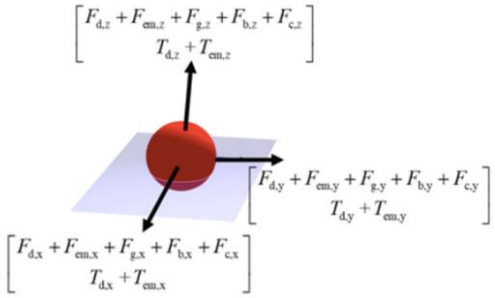

Figure 42 The Forces Acting on the Swimmer in x y z Coordinates

In the simulation, a single coil in the Y-axis was operated by applying a current of 2 amperes. The swimmer was pulled towards the coil in the y-direction. When a current of 2 amperes is applied on a single coil, the robot's time-dependent velocity and displacement graph are shown in figure 43.

The swimmer movement starts from the point (x,y) = (0,0), and the rigid body speed increases as it gets closer to the current passing coil. Likewise, the magnetic

field intensity in the axis of motion increases as the swimmer gets closer to the current flowing coil.

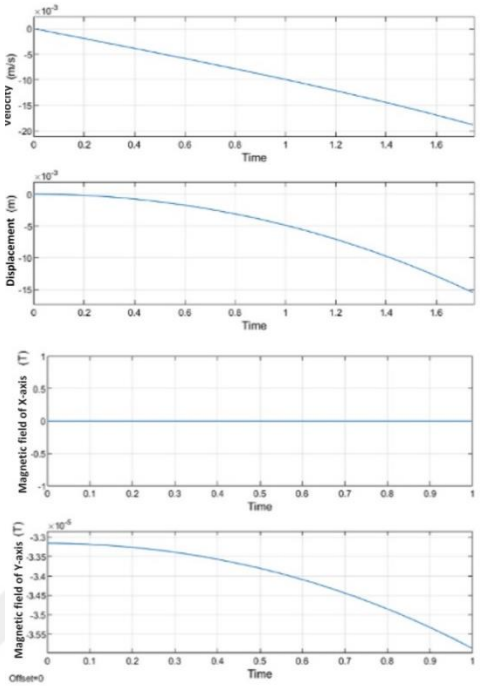

Figure 43 Time-dependent Velocity and Displacement Graphs

5 CONCLUSIONS

In this project, functionalized 3D printed milli-swimmers were successfully produced with photosensitive resin conjugated magnetic materials using a 3D printer (SLA). Fe flakes, Nd-F-B microparticles, and Fe nanoparticles were chosen to actuate milli-swimmers under an external magnetic field gradient. The movements of milli-swimmers were actuated by an electromagnetic coil system. Even though swimmers have diverse structures and sizes, Fe flake particles have the best motion performance due to their magnetic susceptibility. In addition, it is seen that it provides more effective results in hyperthermia applications.

One of the aims of this project is to develop the potential of milli-swimmers with low-cost and time-efficient printing to determine swimming performances in a closed environment. It has also been indicated that the possibility of rapid design will be advantageous when optimizing the printing of various structures not only at the small-scale swimmers but also at channels, molds, and experiment apparatus. Furthermore, Milli-swimmers have successfully steered in PDMS and resin-based channels. Which are reusable and offer a lab-on-a-chip design suitable for the biological environment. Detection of the swimmers was accomplished with the real-time object tracking algorithms.

Finally, the data collected during the thesis stage were presented at international conferences in MMM 2020 and INTERMAG 2021 and published two articles (DOI:10.1016/j.heliyon.2019.e03124 and DOI: 10.1016/j.jmmm.2021.168976).

6 FUTURE WORK

Competencies for the swimmers' magnetic actuation and hyperthermia applications can be developed by using different biocompatible magnetic materials in smaller sizes. In the light of this thesis, the utilization areas of induction heating treatment can be expanded by combining different materials and their properties. Micro and nanometer-sized particles tailored to utilize in hyperthermia and drug delivery applications will be prepared at various concentrations and tested on cells. Further expectations are intended to optimize the behavior of magnetic particle-integrated swimmers in the vascular system and observe their in-vivo effects on glial brain tumor cells.

Moreover, the electromagnetic system will be updated to offer superior tracking and detection implementations. (figure 16) According to the real-time swimmer detection system, a closed epoxy glass system will be made to enhance the light source so that the algorithm can better detect the swimmer in the environment and prevent vibrations in the pool.

REFERENCES

Aarønæs, A. S., & Nilsson, H. (2014). *Dynamic response of pipe rack steel structures to explosion loads*.

Abbott, J. J., Peyer, K. E., Lagomarsino, M. C., Zhang, L., Dong, L., Kaliakatsos, I. K., & Nelson, B. J. (2009). How should microrobots swim? *International Journal of Robotics Research*, *28*(11–12), 1434–1447. https://doi.org/10.1177/0278364909341658

Abenojar, E. C., Wickramasinghe, S., Bas-Concepcion, J., & Samia, A. C. S. (2016). Structural effects on the magnetic hyperthermia properties of iron oxide nanoparticles. *Progress in Natural Science: Materials International*, *26*(5), 440–448. https://doi.org/10.1016/j.pnsc.2016.09.004

Aharoni, A. (2001). *Introduction to the Theory of Ferromagnetism (International Series of Monographs on Physics, 109)*(2nd ed.). Clarendon Press.

Ahn, C., Liang, X., & Cai, S. (2019). Bioinspired Design of Light-Powered Crawling, Squeezing, and Jumping Untethered Soft Robot. *Advanced Materials Technologies*, *4*(7), 1–9. https://doi.org/10.1002/admt.201900185

Akdogan, N. G., Hadjipanayis, G. C., & Sellmyer, D. J. (2009). Anisotropic Sm-(Co,Fe) nanoparticles by surfactant-assisted ball milling. *Journal of Applied Physics*, *105*(7), 1–4. https://doi.org/10.1063/1.3067851

Alapan, Y., Bozuyuk, U., Erkoc, P., Karacakol, A. C., & Sitti, M. (2020). Multifunctional surface microrollers for targeted cargo delivery in physiological blood flow. *Science Robotics*, *5*(42), eaba5726. https://doi.org/10.1126/scirobotics.aba5726

Alapan, Y., Bozuyuk, U., Erkoc, P., & Sitti, M. (2020). *Multifunctional Surface Microrollers for Targeted Cargo Delivery in Blood Flow*. *May*, 1–36. https://doi.org/10.1126/scirobotics.aba5726

Alapan, Y., Matsuyama, Y., Little, J. A., & Gurkan, U. A. (2016). Dynamic deformability of sickle red blood cells in microphysiological flow. *Technology*, *4*(2), 71–79. https://doi.org/10.1142/S2339547816400045

Alapan, Y., Yasa, O., Schauer, O., Giltinan, J., Tabak, A. F., Sourjik, V., & Sitti, M. (2018). Soft erythrocyte-based bacterial microswimmers for cargo delivery. *Science Robotics*, *3*(17), eaar4423. https://doi.org/10.1126/scirobotics.aar4423

Al-Shammari, H. A., Akdogan, N. G. G., Erkoc, P., Akdogan, O., Alshammari, H. A., Akdogan, N. G. G., Erkoc, P., Akdogan, O., Al-Shammari, H. A., Akdogan, N. G. G., Erkoc, P., & Akdogan, O. (2021). Synthesis of Magneto-Responsive Microswimmers for Biomedical Applications. *AIP Advances*, *11*(2), 025312. https://doi.org/10.1063/9.0000103

Amit, Y., Felzenszwalb, P., & Girshick, R. (2020). Object Detection. *Computer Vision*, 1–9. https://doi.org/10.1007/978-3-030-03243-2_660-1

Anderson, K. B., Lockwood, S. Y., Martin, R. S., & Spence, D. M. (2013). A 3D printed fluidic device that enables integrated features. *Analytical Chemistry*, *85*(12), 5622–5626. https://doi.org/10.1021/ac4009594

Arcese, L., Fruchard, M., Ferreira, A., Arcese, L., Fruchard, M., Ferreira, A., Controller, A., Microrobot, M., Arcese, L., Fruchard, M., & Ferreira, A. (2013). *Microrobot To cite this version : HAL Id : hal-00811642*.

Arruebo, M., Vilaboa, N., Sáez-Gutierrez, B., Lambea, J., Tres, A., Valladares, M., & González-Fernández, Á. (2011). Assessment of the evolution of cancer

treatment therapies. *Cancers*, *3*(3), 3279–3330. https://doi.org/10.3390/cancers3033279

Avolio, M., Gavilán, H., Mazario, E., Brero, F., Arosio, P., Lascialfari, A., & Puerto Morales, M. (2019). Elongated magnetic nanoparticles with high-aspect ratio: A nuclear relaxation and specific absorption rate investigation. *Physical Chemistry Chemical Physics*, *21*(34), 18741–18752. https://doi.org/10.1039/c9cp03441b

Bahadorimehr, A. R., Jumril, Y., & Majlis, B. Y. (2010). Low cost fabrication of microfluidic microchannels for Lab-On-a-Chip applications. *2010 International Conference on Electronic Devices, Systems and Applications, ICEDSA 2010 - Proceedings*, 242–244. https://doi.org/10.1109/ICEDSA.2010.5503067

Barba-Guaman, L., Calderon-Cordova, C., & Quezada-Sarmiento, P. A. (2017). Detección de objetos en movimiento a través de la umbralización del color. *Iberian Conference on Information Systems and Technologies, CISTI, May 2019*. https://doi.org/10.23919/CISTI.2017.7975755

Başağaoğlu, H., Succi, S., Wyrick, D., & Blount, J. (2018). Particle Shape Influences Settling and Sorting Behavior in Microfluidic Domains. *Scientific Reports*, *8*(1), 1–11. https://doi.org/10.1038/s41598-018-26786-7

Beg, S., Almalki, W. H., Malik, A., Farhan, M., Aatif, M., Rahman, Z., Alruwaili, N. K., Alrobaian, M., Tarique, M., & Rahman, M. (2020). 3D printing for drug delivery and biomedical applications. *Drug Discovery Today*, *25*(9), 1668–1681. https://doi.org/10.1016/j.drudis.2020.07.007

Beik, J., Abed, Z., Ghoreishi, F. S., Hosseini-Nami, S., Mehrzadi, S., Shakeri-Zadeh, A., & Kamrava, S. K. (2016). Nanotechnology in hyperthermia cancer therapy: From fundamental principles to advanced applications. *Journal of Controlled Release*, *235*, 205–221. https://doi.org/10.1016/j.jconrel.2016.05.062

Beiranvand, R. (2013). Analyzing the uniformity of the generated magnetic field by a practical one-dimensional Helmholtz coils system. *Review of Scientific Instruments*, *84*(7). https://doi.org/10.1063/1.4813275

Beković, M., & Hamler, A. (2010). Determination of the heating effect of magnetic fluid in alternating magnetic field. *IEEE Transactions on Magnetics*, *46*(2), 552–555. https://doi.org/10.1109/TMAG.2009.2033944

Belyanina, I., Kolovskaya, O., Zamay, S., Gargaun, A., Zamay, T., & Kichkailo, A. (2017). Targeted magnetic nanotheranostics of cancer. *Molecules*, *22*(6), 1–19. https://doi.org/10.3390/molecules22060975

Billiet, T., Vandenhaute, M., Schelfhout, J., Van Vlierberghe, S., & Dubruel, P. (2012). A review of trends and limitations in hydrogel-rapid prototyping for tissue engineering. *Biomaterials*, *33*(26), 6020–6041. https://doi.org/10.1016/j.biomaterials.2012.04.050

Bordelon, D. E., Goldstein, R. C., Nemkov, V. S., Kumar, A., Jackowski, J. K., Deweese, T. L., & Ivkov, R. (2012). *Magnetic Fields With Enhanced Uniformity for Biomedical Applications*. *48*(1), 47–52.

Ceylan, H., Giltinan, J., Kozielski, K., & Sitti, M. (2017). Mobile microrobots for bioengineering applications. *Lab on a Chip*, *17*(10), 1705–1724. https://doi.org/10.1039/c7lc00064b

Ceylan, H., Yasa, I. C., Yasa, O., Tabak, A. F., Giltinan, J., & Sitti, M. (2019). 3D-Printed Biodegradable Microswimmer for Theranostic Cargo Delivery and Release [Research-article]. *ACS Nano*, *13*(3), 3353–3362. https://doi.org/10.1021/acsnano.8b09233

Chen, C., Mehl, B. T., Munshi, A. S., Townsend, A. D., Spence, D. M., & Martin, R. S. (2016). 3D-printed microfluidic devices: fabrication, advantages and limitations - a mini review. *Analytical Methods*, *8*(31), 6005–6012. https://doi.org/10.1039/c6ay01671e

Chen, X. Z., Jang, B., Ahmed, D., Hu, C., De Marco, C., Hoop, M., Mushtaq, F., Nelson, B. J., & Pané, S. (2018). Small-Scale Machines Driven by External Power Sources. *Advanced Materials*, *30*(15), 1–22. https://doi.org/10.1002/adma.201705061

Coïsson, M., Barrera, G., Celegato, F., Martino, L., Kane, S. N., Raghuvanshi, S., Vinai, F., & Tiberto, P. (2017). Hysteresis losses and specific absorption rate measurements in magnetic nanoparticles for hyperthermia applications. *Biochimica et Biophysica Acta - General Subjects*, *1861*(6), 1545–1558. https://doi.org/10.1016/j.bbagen.2016.12.006

Cregg, P. J., Murphy, K., & Mardinoglu, A. (2012). Inclusion of interactions in mathematical modelling of implant assisted magnetic drug targeting. *Applied Mathematical Modelling*, *36*(1), 1–34. https://doi.org/10.1016/j.apm.2011.05.036

Cruz, M. M., Ferreira, L. P., Alves, A. F., Mendo, S. G., Ferreira, P., Godinho, M., & Carvalho, M. D. (2017). Nanoparticles for Magnetic Hyperthermia Chapter Outline. In *Nanostructures for Cancer Therapy*. Elsevier Inc. https://doi.org/10.1016/B978-0-323-46144-3/00019-2

Darmawan, B. A., Li, H., Nguyen, K. T., Kim, S. J., Kim, S., Kim, C. S., Park, J. O., & Choi, E. (2019). Simple fabrication of helical-shaped microrobot with NdFeB nanoparticle by self-rolling technique. *Proceedings of MARSS 2019: 4th International Conference on Manipulation, Automation, and Robotics at Small Scales*. https://doi.org/10.1109/MARSS.2019.8860955

Deatsch, A. E., & Evans, B. A. (2014). Heating efficiency in magnetic nanoparticle hyperthermia. *Journal of Magnetism and Magnetic Materials*, *354*, 163–172. https://doi.org/10.1016/j.jmmm.2013.11.006

Domac, B. H., AlKhatib, S., Zirhli, O., Akdogan, N. G., Öçal Dirican, C., Bulut, G., & Akdogan, O. (2020). Effects of PEGylated Fe–Fe3O4 core-shell nanoparticles on NIH3T3 and A549 cell lines. *Heliyon*, *6*(1), 4–9. https://doi.org/10.1016/j.heliyon.2019.e03124

Dörr, A., & Hardt, S. (2015). Driven particles at fluid interfaces acting as capillary dipoles. *Journal of Fluid Mechanics*, *770*, 5–26. https://doi.org/10.1017/jfm.2015.129

Dworzanski, J. P., & Meuzelaar, H. L. C. (2016). Pyrolysis mass spectrometry, methods. In *Encyclopedia of Spectroscopy and Spectrometry* (3rd ed.). Elsevier Ltd. https://doi.org/10.1016/B978-0-12-409547-2.11686-5

Eigenbrod, M., & Hardt, S. (2020). The effective shear and dilatational viscosities of a particle-laden interface in the dilute limit. *Journal of Fluid Mechanics*, *903*, A26. https://doi.org/10.1017/jfm.2020.627

El-Boubbou, K. (2018). Magnetic iron oxide nanoparticles as drug carriers: Clinical relevance. *Nanomedicine*, *13*(8), 953–971. https://doi.org/10.2217/nnm-2017-0336

Erkoc, P., Odeh, Y. N., Alrifai, N., Zirhli, O., Gunduz Akdogan, N., Yildiz, B., Misirlioglu, I. B., & Akdogan, O. (2020). Photocurable pentaerythritol triacrylate/lithium phenyl-2,4,6-trimethylbenzoylphosphinate-based ink for

extrusion-based 3D printing of magneto-responsive materials. *Journal of Applied Polymer Science*, *January*, 1–10. https://doi.org/10.1002/app.49043
Fantino, E., Chiappone, A., Roppolo, I., Manfredi, D., Bongiovanni, R., Pirri, C. F., & Calignano, F. (2016). 3D Printing of Conductive Complex Structures with in Situ Generation of Silver Nanoparticles. *Advanced Materials*, *28*(19), 3712–3717. https://doi.org/10.1002/adma.201505109
Fischer, P., & Ghosh, A. (2011). Magnetically actuated propulsion at low Reynolds numbers: Towards nanoscale control. *Nanoscale*, *3*(2), 557–563. https://doi.org/10.1039/c0nr00566e
Fukuda, T., Kawamoto, A., Arai, F., & Matsuura, H. (1994). Mechanism and swimming experiment of micro mobile robot in water. *Proceedings - IEEE International Conference on Robotics and Automation*, *pt 1*, 814–819. https://doi.org/10.1109/robot.1994.351388
Gallego-Urrea, J. A., Tuoriniemi, J., & Hassellöv, M. (2011). Applications of particle-tracking analysis to the determination of size distributions and concentrations of nanoparticles in environmental, biological and food samples. *TrAC - Trends in Analytical Chemistry*, *30*(3), 473–483. https://doi.org/10.1016/j.trac.2011.01.005
GILCHRIST, R. K., MEDAL, R., SHOREY, W. D., HANSELMAN, R. C., PARROTT, J. C., & TAYLOR, C. B. (1957). Selective inductive heating of lymph nodes. *Annals of Surgery*, *146*(4), 596–606. https://doi.org/10.1097/00000658-195710000-00007
Goldman, A. (1999). *Handbook of Modern Ferromagnetic Materials*. Springer, Boston, MA. https://doi.org/https://doi.org/10.1007/978-1-4615-4917-8
Goudu, S. R., Yasa, I. C., Hu, X., Ceylan, H., Hu, W., & Sitti, M. (2020). Biodegradable Untethered Magnetic Hydrogel Milli-Grippers. *Advanced Functional Materials*, *2004975*. https://doi.org/10.1002/adfm.202004975
Griffiths, David J; College, R. (1999). *Introduction to Electrodinamic* (p. 599). Cambridge University Press.
Gutfleisch, O., Willard, M. A., Brück, E., Chen, C. H., Sankar, S. G., & Liu, J. P. (2011). Magnetic materials and devices for the 21st century: Stronger, lighter, and more energy efficient. *Advanced Materials*, *23*(7), 821–842. https://doi.org/10.1002/adma.201002180
Hamley, I. W. (2003). Nanotechnologie mit weichen Materialien. *Angewandte Chemie*, *115*(15), 1730–1752. https://doi.org/10.1002/ange.200200546
Hedayatnasab, Z., Abnisa, F., & Daud, W. M. A. W. (2017). Review on magnetic nanoparticles for magnetic nanofluid hyperthermia application. *Materials and Design*. https://doi.org/10.1016/j.matdes.2017.03.036
Hira Domac, B., Alshammari, H. A., Gunduz Akdogan, N., & Akdogan, O. (2021). Development and characterization of magnetically actuated milli-swimmers by Stereolithography. *Journal of Magnetism and Magnetic Materials*, *548*(November 2021), 168976. https://doi.org/10.1016/j.jmmm.2021.168976
Hongbin, Y., Guangya, Z., Siong, C. F., Shouhua, W., & Feiwen, L. (2009). Novel polydimethylsiloxane (PDMS) based microchannel fabrication method for lab-on-a-chip application. *Sensors and Actuators, B: Chemical*, *137*(2), 754–761. https://doi.org/10.1016/j.snb.2008.11.035
Hosseinabadi, S., Jafari, M. J., Kokabi, M., & Mohseni, M. (2020). Improving the electromagnetic shielding of fabricated NdFeB particles by a coating thin

carbonaceous layer. *Chemical Physics Letters*, *739*, 137015. https://doi.org/10.1016/j.cplett.2019.137015

Hossen, S., Hossain, M. K., Basher, M. K., Mia, M. N. H., Rahman, M. T., & Uddin, M. J. (2019). Smart nanocarrier-based drug delivery systems for cancer therapy and toxicity studies: A review. In *Journal of Advanced Research* (Vol. 15). Cairo University. https://doi.org/10.1016/j.jare.2018.06.005

Hu, W., Lum, G. Z., Mastrangeli, M., & Sitti, M. (2018). Small-scale soft-bodied robot with multimodal locomotion. *Nature*, *554*(7690), 81–85. https://doi.org/10.1038/nature25443

Hull, C. W. (1984). Apparatus for Production of Three-Dmensonal Objects By Stereo Thography. *Patent*, *19*, 16.

Hussain, M., Zhao, L. Z., Zhang, C., Jiao, D. L., Zhong, X. C., & Liu, Z. W. (2016). Composition-dependent magnetic properties of melt-spun la or/and Ce substituted nanocomposite NdFeB alloys. *Physica B: Condensed Matter*, *483*, 69–74. https://doi.org/10.1016/j.physb.2015.12.033

Johnson, R. E., & Brokaw, C. J. (1979). Flagellar hydrodynamics. A comparison between resistive-force theory and slender-body theory. *Biophysical Journal*, *25*(1), 113–127. https://doi.org/10.1016/S0006-3495(79)85281-9

Jordan, A., Maier-Hauff, K., Wust, P., Rau, B., & Johannsen, M. (2007). Thermotherapie mit magnetischen nanopartikeln. *Onkologe*, *13*(10), 894–902. https://doi.org/10.1007/s00761-007-1263-3

Jun, Y.-W., Seo, J.-W., & Cheon, J. (2008). ChemInform Abstract: Nanoscaling Laws of Magnetic Nanoparticles and Their Applicabilities in Biomedical Sciences. *ChemInform*, *39*(22). https://doi.org/10.1002/chin.200822266

Khan, M. A. M., Kumar, S., Ahamed, M., Alrokayan, S. A., & AlSalhi, M. S. (2011). Structural and thermal studies of silver nanoparticles and electrical transport study of their thin films. *Nanoscale Research Letters*, *6*, 1–8. https://doi.org/10.1186/1556-276X-6-434

Khurshid, H., Alonso, J., Nemati, Z., Phan, M. H., Mukherjee, P., Fdez-Gubieda, M. L., Barandiarán, J. M., & Srikanth, H. (2015). Anisotropy effects in magnetic hyperthermia: A comparison between spherical and cubic exchange-coupled FeO/Fe3O4 nanoparticles. *Journal of Applied Physics*, *117*(17). https://doi.org/10.1063/1.4919250

Khurshid, H., Li, W., Chandra, S., Phan, M. H., Hadjipanayis, G. C., Mukherjee, P., & Srikanth, H. (2013). Mechanism and controlled growth of shape and size variant core/shell FeO/Fe3O4 nanoparticles. *Nanoscale*, *5*(17), 7942–7952. https://doi.org/10.1039/c3nr02596a

Kim, K. S., & Park, J. K. (2005). Magnetic force-based multiplexed immunoassay using superparamagnetic nanoparticles in microfluidic channel. *Lab on a Chip*, *5*(6), 657–664. https://doi.org/10.1039/b502225h

Kim, S. H., & Ishiyama, K. (2014). Magnetic robot and manipulation for active-locomotion with targeted drug release. *IEEE/ASME Transactions on Mechatronics*, *19*(5), 1651–1659. https://doi.org/10.1109/TMECH.2013.2292595

Kim, S., Kim, S., Majditehran, H., Patel, D. K., Majidi, C., & Bergbreiter, S. (2020). Electromechanical Characterization of 3D Printable Conductive Elastomer for Soft Robotics. *2020 3rd IEEE International Conference on Soft Robotics, RoboSoft 2020*, 318–324. https://doi.org/10.1109/RoboSoft48309.2020.9116027

Kirvin, A., Gregory, D., Parnell, A., Campbell, A. I., & Ebbens, S. (2021). Rotating ellipsoidal catalytic micro-swimmers via glancing angle evaporation . *Materials Advances*, *2*(21), 7045–7053. https://doi.org/10.1039/d1ma00533b

Kitson, P. J., Rosnes, M. H., Sans, V., Dragone, V., & Cronin, L. (2012). Configurable 3D-Printed millifluidic and microfluidic "lab on a chip" reactionware devices. *Lab on a Chip*, *12*(18), 3267–3271. https://doi.org/10.1039/c2lc40761b

Kobayashi, T. (2011). Cancer hyperthermia using magnetic nanoparticles. *Biotechnology Journal*, *6*(11), 1342–1347. https://doi.org/10.1002/biot.201100045

Koleoso, M., Feng, X., Xue, Y., Li, Q., Munshi, T., & Chen, X. (2020). Micro/nanoscale magnetic robots for biomedical applications. *Materials Today Bio*, *8*(August). https://doi.org/10.1016/j.mtbio.2020.100085

Kriegman, S., Blackiston, D., Levin, M., & Bongard, J. (2020). A scalable pipeline for designing reconfigurable organisms. *Proceedings of the National Academy of Sciences of the United States of America*, *117*(4), 1853–1859. https://doi.org/10.1073/pnas.1910837117

Lee, Y., Ceylan, H., Yasa, I. C., Kilic, U., & Sitti, M. (2020). *3D-Printed Multi-Stimuli-Responsive Mobile Micromachines*. https://doi.org/10.1021/acsami.0c18221

Lehmann, J. F., Guy, A. W., Stonebridge, J. B., & Lateur, B. J. (1978). Evaluation of a Therapeutic Direct-Contact 915-MHz Microwave Applicator for Effective Deep-Tissue Heating in Humans. *IEEE Transactions on Microwave Theory and Techniques*, *26*(8), 556–563. https://doi.org/10.1109/TMTT.1978.1129438

Liu, H., & Mo, J. (2010). Study on nanosilica reinforced stereolithography resin. *Journal of Reinforced Plastics and Composites*, *29*(6), 909–920. https://doi.org/10.1177/0731684409102838

Llacer-Wintle, J., Rivas-Dapena, A., Chen, X. Z., Pellicer, E., Nelson, B. J., Puigmartí-Luis, J., & Pané, S. (2021). Biodegradable Small-Scale Swimmers for Biomedical Applications. *Advanced Materials*, *33*(42), 1–22. https://doi.org/10.1002/adma.202102049

Lu, H., Zhang, M., Yang, Y., Huang, Q., Fukuda, T., Wang, Z., & Shen, Y. (2018). A bioinspired multilegged soft millirobot that functions in both dry and wet conditions. *Nature Communications*, *9*(1). https://doi.org/10.1038/s41467-018-06491-9

M., M., Bahadar, S., Jamal, A., Faisal, M., & M., A. (2011). Iron Oxide Nanoparticles. *Nanomaterials*. https://doi.org/10.5772/27698

Malvindi, M. A., de Matteis, V., Galeone, A., Brunetti, V., Anyfantis, G. C., Athanassiou, A., Cingolani, R., & Pompa, P. P. (2014). Toxicity assessment of silica coated iron oxide nanoparticles and biocompatibility improvement by surface engineering. *PLoS ONE*, *9*(1), 1–11. https://doi.org/10.1371/journal.pone.0085835

Marco, G. (2015). Low cost inkjet printing for the fast prototyping of surface EMG detection systems. *2015 IEEE International Symposium on Medical Measurements and Applications, MeMeA 2015 - Proceedings*, 79–83. https://doi.org/10.1109/MeMeA.2015.7145176

Mehta, V., & Rath, S. N. (2021). 3D printed microfluidic devices: a review focused on four fundamental manufacturing approaches and implications on the field of

healthcare. *Bio-Design and Manufacturing*, *4*(2), 311–343. https://doi.org/10.1007/s42242-020-00112-5

Melchels, F. P. W., Feijen, J., & Grijpma, D. W. (2010). A review on stereolithography and its applications in biomedical engineering. *Biomaterials*, *31*(24), 6121–6130. https://doi.org/10.1016/j.biomaterials.2010.04.050

Natividad, E., Castro, M., & Mediano, A. (2008). Accurate measurement of the specific absorption rate using a suitable adiabatic magnetothermal setup. *Applied Physics Letters*, *92*(9), 2008–2010. https://doi.org/10.1063/1.2891084

Nelson, B. J., Kaliakatsos, I. K., & Abbott, J. J. (2010). Microrobots for minimally invasive medicine. *Annual Review of Biomedical Engineering*, *12*, 55–85. https://doi.org/10.1146/annurev-bioeng-010510-103409

Niemirowicz, K., Markiewicz, K. H., Wilczewska, A. Z., & Car, H. (2012). Magnetic nanoparticles as new diagnostic tools in medicine. *Advances in Medical Sciences*, *57*(2), 196–207. https://doi.org/10.2478/v10039-012-0031-9

Ningthoujam, R. S., Vatsa, R. K., Kumar, A., & Pandey, B. N. (2012). Functionalized magnetic nanoparticles: Concepts, synthesis and application in cancer hyperthermia. In *Functional Materials*. Elsevier Inc. https://doi.org/10.1016/B978-0-12-385142-0.00006-4

Ozunlu, S., Akdogan, N. G., Bozkurt, M. N., Doganturk, L., Alshammari, H. A., le Roy, D., & Akdogan, O. (2021). Innovative technique for patterning Nd–Fe–B arrays and development of a microfluidic device with high trapping efficiency. *Nanotechnology*, *32*(49), 495501. https://doi.org/10.1088/1361-6528/ac1dd6

P., A. V., L., A. M., J., E. J., K., R., D., Q. S. T., Fernandez, A. christina, S., K., & S., J. Das. (2016). Investigation of optical, electrical and magnetic properties of cobalt ferrite nanoparticles by naive co-precipitation technique. *Optik*, *127*(20), 9917–9925. https://doi.org/10.1016/j.ijleo.2016.07.063

Palagi, S., Singh, D. P., & Fischer, P. (2019). Light-Controlled Micromotors and Soft Microrobots. *Advanced Optical Materials*, *7*(16), 1–18. https://doi.org/10.1002/adom.201900370

Parkinson, G. S. (2016). Iron oxide surfaces. *Surface Science Reports*, *71*(1), 272–365. https://doi.org/10.1016/j.surfrep.2016.02.001

Patil, R. M., Thorat, N. D., Shete, P. B., Otari, S. v., Tiwale, B. M., & Pawar, S. H. (2016). In vitro hyperthermia with improved colloidal stability and enhanced SAR of magnetic core/shell nanostructures. *Materials Science and Engineering C*, *59*, 702–709. https://doi.org/10.1016/j.msec.2015.10.064

Pawashe, C., Floyd, S., & Sitti, M. (2009). Modeling and experimental characterization of an untethered magnetic micro-robot. *International Journal of Robotics Research*, *28*(8), 1077–1094. https://doi.org/10.1177/0278364909341413

Peer, D., Karp, J. M., Hong, S., Farokhzad, O. C., Margalit, R., & Langer, R. (2007). 84 Nat nanotech 2007 R Langer Nanocarriers as an emerging platform for cancer therapy.pdf. *Nature Nanotechnology*, *2*, 751–760. https://doi.org/10.1038/nnano.2007.387

Pepperhoff, W., & Acet, M. (2001). The structure of iron. In *Constitution and Magnetism of Iron and its Alloys* (pp. 1–13). Springer Berlin Heidelberg. https://doi.org/10.1007/978-3-662-04345-5_1

Périgo, E. A., Hemery, G., Sandre, O., Ortega, D., Garaio, E., Plazaola, F., & Teran, F. J. (2015). Fundamentals and advances in magnetic hyperthermia. *Applied Physics Reviews*, *2*(4). https://doi.org/10.1063/1.4935688

Périgo, E. A., Silva, S. C., de Sousa, E. M. B., Freitas, A. A., Cohen, R., Nagamine, L. C. C. M., Takiishi, H., & Landgraf, F. J. G. (2012). Properties of nanoparticles prepared from NdFeB-based compound for magnetic hyperthermia application. *Nanotechnology*, *23*(17). https://doi.org/10.1088/0957-4484/23/17/175704

Peyer, K. E., Zhang, L., & Nelson, B. J. (2013). Bio-inspired magnetic swimming microrobots for biomedical applications. *Nanoscale*, *5*(4), 1259–1272. https://doi.org/10.1039/c2nr32554c

Pollefliet, J. (2018). Applications of Power Electronics. In *Power Electronics*. https://doi.org/10.1016/b978-0-12-814643-9.50015-5

Popescu, R. C., Andronescu, E., & Vasile, B. S. (2019). Recent advances in magnetite nanoparticle functionalization for nanomedicine. *Nanomaterials*, *9*(12), 1–31. https://doi.org/10.3390/nano9121791

Puisto, A., Illa, X., Mohtaschemi, M., & Alava, M. J. (2012). Modeling the viscosity and aggregation of suspensions of highly anisotropic nanoparticles. *European Physical Journal E*, *35*(1), 1–7. https://doi.org/10.1140/epje/i2012-12006-1

Purcell, E. M. (1977). Life at low Reynolds number. *American Journal of Physics*, *45*(1), 3–11. https://doi.org/10.1119/1.10903

Raj, J. R., & Srinivasulu, S. (2021). Object detection in live streaming video using deep learning approach. *IOP Conference Series: Materials Science and Engineering*, *1020*(1). https://doi.org/10.1088/1757-899X/1020/1/012028

Ramos-Docampo, M. A., Fernández-Medina, M., Taipaleenmäki, E., Hovorka, O., Salgueirinõ, V., & Städler, B. (2019). Microswimmers with Heat Delivery Capacity for 3D Cell Spheroid Penetration. *ACS Nano*, *13*(10), 12192–12205. https://doi.org/10.1021/acsnano.9b06869

Rani, G., & Jindal, A. (2020). *Real-Time Object Detection and Tracking Using Velocity Control BT - Smart Systems and IoT: Innovations in Computing* (A. K. Somani, R. S. Shekhawat, A. Mundra, S. Srivastava, & V. K. Verma, Eds.; pp. 767–778). Springer Singapore.

Rao, G. V. S. J., Prasad, T. N. V. K. V., Shameer, S., & Rao, M. P. (2018). Soapnut extract mediated synthesis of nanoscale cobalt substituted NdFeB ferromagnetic materials and their characterization. *Journal of Magnetism and Magnetic Materials*, *451*, 159–166. https://doi.org/10.1016/j.jmmm.2017.11.009

Rueden, C. T., Schindelin, J., Hiner, M. C., DeZonia, B. E., Walter, A. E., Arena, E. T., & Eliceiri, K. W. (2017). ImageJ2: ImageJ for the next generation of scientific image data. *BMC Bioinformatics*, *18*(1), 1–26. https://doi.org/10.1186/s12859-017-1934-z

Sanchez, S., Solovev, A. A., Harazim, S. M., & Schmidt, O. G. (2011a). Microbots swimming in the flowing streams of microfluidic channels. *Journal of the American Chemical Society*, *133*(4), 701–703. https://doi.org/10.1021/ja109627w

Sanchez, S., Solovev, A. A., Harazim, S. M., & Schmidt, O. G. (2011b). *Swim in Micro channel !.pdf*. 701–703.

Shallan, A. I., Smejkal, P., Corban, M., Guijt, R. M., & Breadmore, M. C. (2014). Cost-effective three-dimensional printing of visibly transparent microchips within minutes. *Analytical Chemistry*, *86*(6), 3124–3130. https://doi.org/10.1021/ac4041857

Shen, Y., Zhang, X., Liang, L., Yue, J., Huang, D., Xu, W., Shi, W., Liang, C., & Xu, S. (2020). Mitochondria-targeting supra-carbon dots: Enhanced

photothermal therapy selective to cancer cells and their hyperthermia molecular actions. *Carbon*, *156*, 558–567. https://doi.org/10.1016/j.carbon.2019.09.079
Sitti, M., Ceylan, H., Hu, W., Giltinan, J., Turan, M., Yim, S., & Diller, E. (2015). Biomedical Applications of Untethered Mobile Milli/Microrobots. *Proceedings of the IEEE*, *103*(2), 205–224. https://doi.org/10.1109/JPROC.2014.2385105
Skomski, R., & Sellmyer, D. J. (2009). Anisotropy of rare-earth magnets. *Journal of Rare Earths*, *27*(4), 675–679. https://doi.org/10.1016/S1002-0721(08)60314-2
Smith, R. P., Absolom, D. R., Spelt, J. K., & Neumann, A. W. (1986). Approaches to determine the surface tension of small particles: Equation-of-state considerations. *Journal of Colloid And Interface Science*, *110*(2), 520–532. https://doi.org/10.1016/0021-9797(86)90405-4
Spain, E., & Venkatanarayanan, A. (2014). Review of Physical Principles of Sensing and Types of Sensing Materials. In *Comprehensive Materials Processing* (Vol. 13). Elsevier. https://doi.org/10.1016/B978-0-08-096532-1.01302-9
Spong, M. W., Hutchinson, S., & Vidyasagar, M. (2006). Robot modeling and control. *IEEE Control Systems*, *26*(6), 113–115. https://doi.org/10.1109/MCS.2006.252815
Stanton, M. M., Trichet-Paredes, C., & Sánchez, S. (2015). Applications of three-dimensional (3D) printing for microswimmers and bio-hybrid robotics. *Lab on a Chip*, *15*(7), 1634–1637. https://doi.org/10.1039/c5lc90019k
Stauffer, P. R., Sneed, P. K., Hashemi, H., & Phillips, T. L. (1994). Practical Induction Heating Coil Designs for Clinical Hyperthermia with Ferromagnetic Implants. *IEEE Transactions on Biomedical Engineering*, *41*(1), 17–28. https://doi.org/10.1109/10.277267
Stayton, I., Ma, Y., Gai, H., Liu, X., & Lin, B. (2007). Visualizing chemical interactions in life sciences with wide-field fluorescence microscopy towards the single-molecule level. *TrAC - Trends in Analytical Chemistry*, *26*(10), 980–992. https://doi.org/10.1016/j.trac.2007.09.007
Sun, C., Lee, J. S. H., & Zhang, M. (2008). Magnetic nanoparticles in MR imaging and drug delivery. *Advanced Drug Delivery Reviews*, *60*(11), 1252–1265. https://doi.org/10.1016/j.addr.2008.03.018
Sun, W., Starly, B., Nam, J., & Darling, A. (2005). Bio-CAD modeling and its applications in computer-aided tissue engineering. *CAD Computer Aided Design*, *37*(11), 1097–1114. https://doi.org/10.1016/j.cad.2005.02.002
Sung, H. W. F., & Rudowicz, C. (2003). Physics behind the magnetic hysteresis loop - A survey of misconceptions in magnetism literature. *Journal of Magnetism and Magnetic Materials*, *260*(1–2), 250–260. https://doi.org/10.1016/S0304-8853(02)01339-2
Taukulis, R., Widdrat, M., Kumari, M., Heinke, D., Rumpler, M., Tompa, Uebe, R., Kraupner, A., Cebers, A., Schüler, D., Pósfai, M., Hirt, A. M., & Faivre, D. (2015). Magnetic iron oxide nanoparticles as MRI contrast agents - A comprehensive physical and theoretical study. *Magnetohydrodynamics*, *51*(4), 721–748. https://doi.org/10.22364/mhd.51.4.7
Taylor, G., & A, P. R. S. L. (1951). Analysis of the swimming of microscopic organisms. *Proceedings of the Royal Society of London. Series A. Mathematical and Physical Sciences*, *209*(1099), 447–461. https://doi.org/10.1098/rspa.1951.0218

Tetsuka, H., & Shin, S. R. (2020). Materials and technical innovations in 3D printing in biomedical applications. *Journal of Materials Chemistry B*, *8*(15), 2930–2950. https://doi.org/10.1039/d0tb00034e

Theodore, A., Jeon, K. J., & Wu, C. Y. (2006). Flake particle synthesis from ductile metal particles using a novel high-speed vibratory mill. *KONA Powder and Particle Journal*, *24*(March), 83–92. https://doi.org/10.14356/kona.2006011

Vallabani, N. V. S., & Singh, S. (2018). Recent advances and future prospects of iron oxide nanoparticles in biomedicine and diagnostics. *3 Biotech*, *8*(6), 1–23. https://doi.org/10.1007/s13205-018-1286-z

Villegas, M., Cetinic, Z., Shakeri, A., & Didar, T. F. (2018). Fabricating smooth PDMS microfluidic channels from low-resolution 3D printed molds using an omniphobic lubricant-infused coating. *Analytica Chimica Acta*, *1000*, 248–255. https://doi.org/10.1016/j.aca.2017.11.063

Vishnuram, P., Ramachandiran, G., Ramasamy, S., & Dayalan, S. (2020). A comprehensive overview of power converter topologies for induction heating applications. *International Transactions on Electrical Energy Systems*, *30*(10), 1–33. https://doi.org/10.1002/2050-7038.12554

Wang, X., Qin, X. H., Hu, C., Terzopoulou, A., Chen, X. Z., Huang, T. Y., Maniura-Weber, K., Pané, S., & Nelson, B. J. (2018). 3D Printed Enzymatically Biodegradable Soft Helical Microswimmers. *Advanced Functional Materials*, *28*(45), 1–8. https://doi.org/10.1002/adfm.201804107

Watanabe, M., Yoneda, M., Morohashi, A., Hori, Y., Okamoto, D., Sato, A., Kurioka, D., Nittami, T., Hirokawa, Y., Shiraishi, T., Kawai, K., Kasai, H., & Totsuka, Y. (2013). Effects of Fe3O4 magnetic nanoparticles on A549 cells. *International Journal of Molecular Sciences*, *14*(8), 15546–15560. https://doi.org/10.3390/ijms140815546

Weng, Z., Zhou, Y., Lin, W., Senthil, T., & Wu, L. (2016). Structure-property relationship of nano enhanced stereolithography resin for desktop SLA 3D printer. *Composites Part A: Applied Science and Manufacturing*, *88*, 234–242. https://doi.org/10.1016/j.compositesa.2016.05.035

Willard, M. A., & Franco, V. (2013). The role of microstructure and processing on magnetic properties of materials. *Jom*, *65*(7), 851–852. https://doi.org/10.1007/s11837-013-0621-4

Wu, J. C., Wang, S. P., Wang, Y. H., & Liu, C. (2020). Sensitivity Analysis of Design Parameters in Transverse Flux Induction Heating Device. *IEEE Transactions on Applied Superconductivity*, *30*(4), 1–6. https://doi.org/10.1109/TASC.2020.2973604

Xia, Y., & Whitesides, G. M. (1998). Soft lithography. *Annual Review of Materials Science*, *28*(1), 153–184. https://doi.org/10.1146/annurev.matsci.28.1.153

Xu, H., Medina-Sánchez, M., Maitz, M. F., Werner, C., & Schmidt, O. G. (2020). Sperm Micromotors for Cargo Delivery through Flowing Blood. *ACS Nano*, *14*(3), 2982–2993. https://doi.org/10.1021/acsnano.9b07851

Yan, Y., Jing, W., & Mehrmohammadi, M. (2020). Photoacoustic imaging to track magnetic-manipulated micro-robots in deep tissue. *Sensors (Switzerland)*, *20*(10), 1–12. https://doi.org/10.3390/s20102816

Yang, M. N., Wang, H., Hu, Y. F., Yang, L. Y. M., Maclennan, A., & Yang, B. (2018). Relating atomic local structures and Curie temperature of NdFeB permanent magnets: an X-ray absorption spectroscopic study. *Rare Metals*, *37*(11), 983–988. https://doi.org/10.1007/s12598-017-0918-5

Yasa, I. C., Ceylan, H., Bozuyuk, U., Wild, A. M., & Sitti, M. (2020). Elucidating the interaction dynamics between microswimmer body and immune system for medical microrobots. *Science Robotics*, *5*(43), 1–14. https://doi.org/10.1126/scirobotics.aaz3867

Yesin, K. B., Vollmers, K., & Nelson, B. J. (2006). Modeling and control of untethered biomicrorobots in a fluidic environment using electromagnetic fields. *International Journal of Robotics Research*, *25*(5–6), 527–536. https://doi.org/10.1177/0278364906065389

Yi, G., Chapman, J. N., Brown, D. N., & Harris, I. R. (2002). Intermediate lamellae phase in lightly disproportionated NdFeB-type alloys. *Journal of Magnetism and Magnetic Materials*, *242–245*, 1325–1328. https://doi.org/10.1016/S0304-8853(01)00966-0

Zhu, W., Li, J., Leong, Y. J., Rozen, I., Qu, X., Dong, R., Wu, Z., Gao, W., Chung, P. H., Wang, J., & Chen, S. (2015). 3D-Printed Artificial Microfish. *Advanced Materials*, *27*(30), 4411–4417. https://doi.org/10.1002/adma.201501372

Zirhli, O., Gunduz Akdogan, N., Odeh, Y. N., Misirlioglu, I. B., Devlin, E., & Akdogan, O. (2020). Fabrication and Characterization of Fe16N2 Micro-Flake Powders and Their Extrusion-Based 3D Printing into Permanent Magnet Form. *Advanced Engineering Materials*, *22*(11). https://doi.org/10.1002/adem.202000311

APPENDICES